Bifurcations of symmetric periodic orbits in a four-dimensional Lorenz-like system and their relation to wild chaos

Juan Patiño-Echeverría, Bernd Krauskopf and Hinke M. Osinga
Department of Mathematics, University of Auckland, New Zealand

July 2026

Abstract

Wild chaos is a higher-dimensional form of chaotic dynamics characterized by the robust presence of homoclinic tangencies. It can only arise in vector fields of dimension at least four, or in diffeomorphisms of dimension at least three. We study a four-dimensional Lorenz-like system known to exhibit a wild pseudohyperbolic attractor for a specific parameter point. Its global bifurcation structure in a two-parameter plane has previously been analysed numerically by computing kneading diagrams and Lyapunov spectra computations, revealing dense accumulations of Shilnikov-type homoclinic bifurcations and parameter regions satisfying necessary conditions for wild chaos.

Here, we build on this analysis by finding and continuing the codimension-one bifurcation curves associated with two fundamental symmetric periodic orbits and their asymmetric counterparts. We determine the criticality of symmetry-breaking, period-doubling, fold, and torus bifurcations, and construct the global two-parameter bifurcation diagram in a compactified parameter plane. These bifurcation curves are shown to form a nested structure that organizes both periodic windows and chaotic regions. In particular, they delimit transitions between periodic dynamics, chaotic attractors generated by period-doubling cascades, and wild pseudohyperbolic attractors. While no single bifurcation curve forms a sharp boundary of wild chaos, torus and fold bifurcations of symmetric periodic orbits are found to play a significant role in organizing the nature of attractors in the system; this finding is supported by numerical computation of Lyapunov spectra for said attractors.

1 Introduction

Chaotic systems are ubiquitous in nature, yet not all chaos is created equal. A special form of chaos—known as *wild*—is so robust that no small change to the governing equations can tame it into regular behaviour. Understanding how wild chaos arises requires uncovering the geometric structures that organize it. In this work, we study a four-dimensional extension of the classic Lorenz system, one of the few concrete systems known to exhibit a wild chaotic attractor. We show that two families of periodic orbits with a special spatio-temporal symmetry act as a geometric backbone, shaping the parameter space and mediating the transitions between regular periodic motion, 'classical' chaos, and wild pseudohyperbolic chaos. By tracking these periodic orbits and their bifurcations, we reveal the regions in a two-parameter plane where one finds wild chaos.

We study the four-dimensional Lorenz-like system

$$\left\{\begin{array}{rcl} \dot{x} &=& \sigma(y-x), \\ \dot{y} &=& x(\rho-z)-y, \\ \dot{z} &=& xy-\beta z+\mu w, \\ \dot{w} &=& -\mu z-\beta w, \end{array}\right. \tag{1}$$

with non-negative parameters σ, β, ρ, and μ. System (1) extends the classic three-dimensional Lorenz system [28] by including the additional parameter μ and variable w, as proposed in [33]. Throughout this paper, we fix σ and β to their classical values $\sigma = 10$ and $\beta = 8/3$. When $\mu = 0$, the hyperplane $\{w = 0\}$

is invariant and system (1) reduces on this hyperplane to the classic Lorenz system. Consequently, key properties such as the $\mathbb{Z}_2$-symmetry and the bifurcation structure of the Lorenz system are embedded in the extended model. In particular, codimension-one bifurcations of the classic Lorenz system extend as curves in the (ρ,μ)-plane.

For the particular choice of parameters $(\rho,\mu) = (25,7)$, which we refer to as (ρ^*,μ^*), system (1) exhibits a *wild* chaotic attractor [17]. A wild chaotic attractor combines two characteristic properties. First, it is attracting and robustly chaotic: it has a positive maximal Lyapunov exponent, and this property persists for all small C^1-perturbations of the system. This is known as pseudohyperbolicity; a general mathematical theory of pseudohyperbolic attractors was developed by Turaev and Shilnikov [37]; see also [16, 36] for further details. Second, the existence of homoclinic tangencies between points in the attractor is a C^1-robust property. The robustness of homoclinic tangencies in the C^1-topology requires a vector field of dimension at least four (or, equivalently, a diffeomorphism of dimension at least three) [7, 16, 37, 36]. Therefore, system (1) provides a minimal setting in which to study wild chaotic attractors.

In contrast, pseudohyperbolic attractors can already exist in three-dimensional flows. The most prominent example is the Lorenz attractor, which is pseudohyperbolic over a range of parameter values; see [8, 10] for details. Its pseudohyperbolicity is guaranteed by a strong stable foliation, which allows the dynamics to be reduced to a one-dimensional map. The existence of this foliation is the key assumption of the *geometric Lorenz model*—introduced independently by Afraimovich, Bykov, and Shilnikov [2] and by Guckenheimer and Williams [18, 19]—which captures the essential qualitative features of the Lorenz system and admits a robust chaotic attractor. Tucker [35] proved rigorously, by using computer-assisted methods, that the Lorenz system itself satisfies the conditions of the geometric model, thereby confirming the existence of the Lorenz attractor.

In the classic Lorenz system, or effectively system (1) with $\mu = 0$, one finds the so-called *homoclinic explosion point* at $\rho = \rho_{\mathrm{r}} \approx 13.9265$, which organizes its complicated dynamics [34]. Here, the origin $\mathbf{0}$ is a saddle point of (1), with a one-dimensional unstable manifold $W^u(\mathbf{0})$—consisting of trajectories that converge to $\mathbf{0}$ in backward time. At the homoclinic explosion point, a basic symmetric pair of homoclinic orbits to $\mathbf{0}$ exists. This global bifurcation creates an infinite number of saddle periodic orbits for $\rho > \rho_{\mathrm{r}}$, but does not yet create the Lorenz attractor. In this so-called *preturbulent regime* [21], any typical initial condition ends up at one of a symmetric pair $p^{\pm}$ of attracting equilibria. The Lorenz attractor itself emerges at $\rho = \rho_{\mathrm{E}} \approx 24.0579$, where the two branches of $W^u(\mathbf{0})$ each form a heteroclinic connection with one of a symmetric pair of saddle periodic orbits. We refer to this codimension-one heteroclinic bifurcation as an EtoP connection (for equilibrium to periodic orbit). For increasing ρ, the resulting chaotic attractor coexists with the attracting equilibria $p^{\pm}$ up to a subcritical Hopf bifurcation at $\rho = \rho_{\mathrm{H}} \approx 24.7368$. There, the two saddle periodic orbits shrink onto $p^{\pm}$ and disappear, so that $p^{\pm}$ lose their stability and become saddles for $\rho > \rho_{\mathrm{H}}$. The Lorenz attractor is then the only attractor; it is pseudohyperbolic from ρ_{E} up to $\rho \approx 31.01$, where the strong stable foliation condition is lost [34, 8, 10].

The key new ingredient in system (1) is the parameter μ, which turns the origin into a saddle-focus equilibrium for $\rho > 1$ and $\mu > 0$: its complex eigenvalues $\lambda_{1,2} = -\beta \pm i\mu$ introduce spiraling dynamics near $\mathbf{0}$ and, hence, for $\mu > 0$, all homoclinic orbits to the origin are of 'chaotic' Shilnikov type [23]. In contrast, the origin of the classic Lorenz system has only real eigenvalues, so its homoclinic orbits do not exhibit spiraling dynamics and are never of Shilnikov type. One might expect that for small $\mu > 0$ and ρ in the range where the Lorenz attractor is pseudohyperbolic, a pseudohyperbolic attractor persists in system (1). However, as shown in [17], μ must be sufficiently large before pseudohyperbolic chaotic dynamics is observed. To verify pseudohyperbolicity at (ρ^*,μ^*), Gonchenko, Kazakov, and Turaev [17] introduced a numerical method based on the computation of Lyapunov exponents and their associated covariant Lyapunov vectors, which checks the transversality conditions characterizing pseudohyperbolicity; see Section 5 for our use of this approach. They combined this method with *kneading diagrams* [5] in the (ρ,σ)-plane, which give a topological characterization of the complexity and denseness of Shilnikov-type homoclinic bifurcations. Note that the chosen value $\rho^* = 25$ is slightly smaller than the classic value $\rho = 28$ associated with the Lorenz attractor [28, 34, 2, 35].

In our previous work [31], we investigated how the codimension-one bifurcations of the classic Lorenz

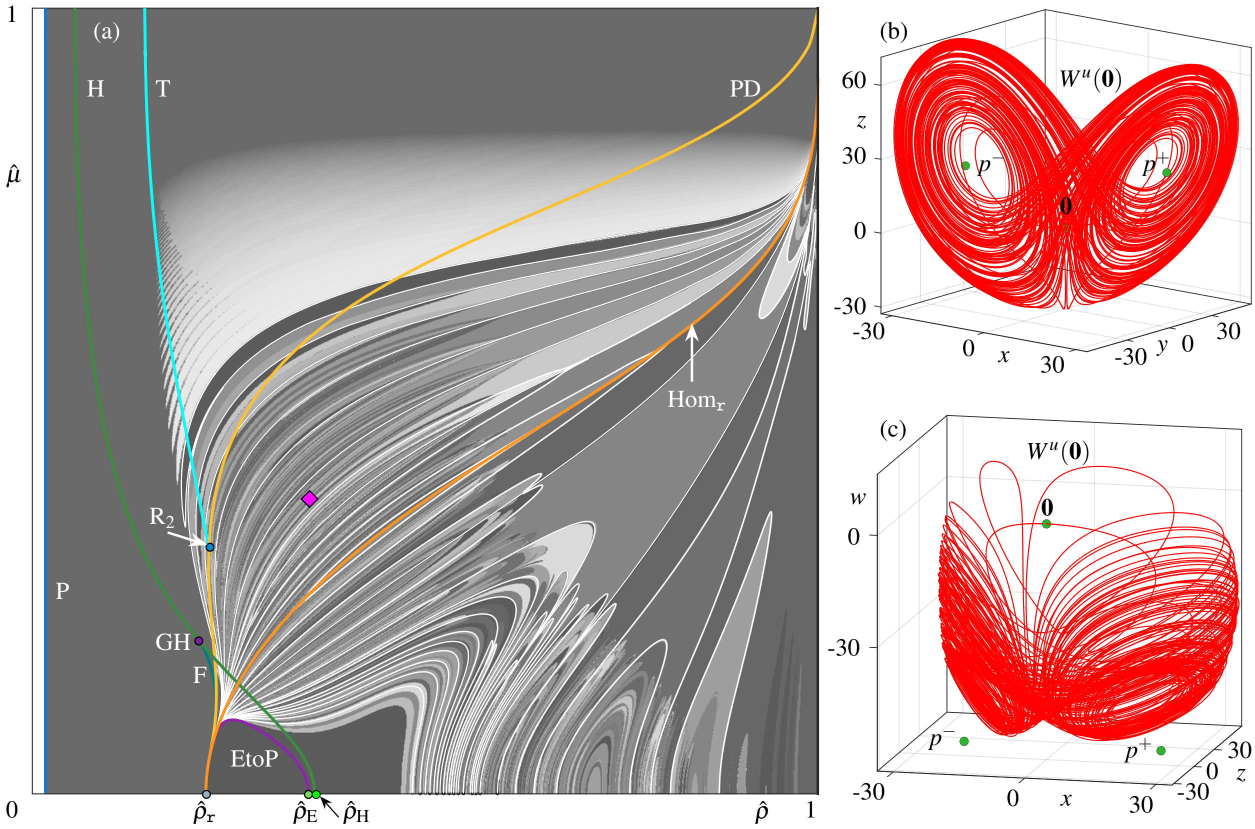

Figure 1: Panel (a) shows the two-parameter bifurcation diagram in the compactified $(\hat{\rho}, \hat{\mu})$-square with the curves P (blue) of pitchfork, H (green) of Hopf, T (cyan) of torus, PD (yellow) of period-doubling, F (teal) of fold of periodic orbits, EtoP (purple) of equilibrium-to-periodic-orbit, and Hom$_{\mathtt{r}}$ (orange) of basic homoclinic bifurcation; also shown are the codimension-two points GH (purple) of generalized Hopf and R$_2$ (blue) of 1:2 resonance bifurcation. The background is shaded by the kneading diagram of K_9, as well as white shades that indicate regions between curves of homoclinic bifurcation with symbol sequences $\mathtt{r}^{n-1}$ and $\mathtt{r}^n$ up to $n = 40$. The magenta diamond marks the point $(\hat{\rho}^*, \hat{\mu}^*) \approx (0.362, 0.394)$ where the wild chaotic attractor was observed in [17]. It is represented by the one-dimensional unstable manifold $W^u(\mathbf{0})$ (red curve) of the saddle equilibrium $\mathbf{0}$ in the projections onto (x, y, z)-space in panel (b) and (x, z, w)-space in panel (c).

system extend as curves into the (ρ, μ)-plane of system (1), with particular emphasis on a region near (ρ^*, μ^*). Figure 1 summarizes these results by showing the resulting bifurcation curves in the compactified coordinates $(\hat{\rho}, \hat{\mu})$ of the unit square in panel (a) with the corresponding point $(\hat{\rho}^*, \hat{\mu}^*)$ marked; the wild chaotic attractor at $(\hat{\rho}^*, \hat{\mu}^*)$, represented by the unstable manifold $W^u(\mathbf{0})$ of $\mathbf{0}$, is shown in projection onto (x, y, z)-space and (x, z, w)-space in panels (b) and (c), respectively. More specifically, the positive quadrant of the (ρ, μ)-plane has been transformed to the unit square in Figure 1(a), so that its right and upper sides correspond to the limits $\rho \to \infty$ and $\mu \to \infty$, respectively; see Section 2.2 for details. The primary homoclinic bifurcation curve Hom$_{\mathtt{r}}$ is the continuation of the basic symmetric pair of homoclinic orbits; it emanates from the homoclinic explosion point at $(\hat{\rho}_{\mathtt{r}}, 0)$ and extends to the corner $(1, 1)$. All curves of homoclinic bifurcation inherited from the classic Lorenz system lie below Hom$_{\mathtt{r}}$ in $\hat{\mu}$, as does the EtoP bifurcation curve, which connects the points $(\hat{\rho}_{\mathrm{E}}, 0)$ and $(\hat{\rho}_{\mathtt{r}}, 0)$ on the $\hat{\rho}$-axis. The point $(\hat{\rho}^*, \hat{\mu}^*)$ in Figure 1(a), lies well above Hom$_{\mathtt{r}}$, which indicates that the EtoP bifurcation is not involved in the creation of the wild chaotic attractor at $(\hat{\rho}^*, \hat{\mu}^*)$. The curve H of Hopf bifurcation begins at $(\hat{\rho}_{\mathrm{H}}, 0)$ and extends in $\hat{\mu}$ with a vertical asymptote. A generalized Hopf bifurcation (GH) changes the criticality of the Hopf bifurcation, and from this point a curve F of fold (or saddle-node) of periodic orbits emerges; as $\hat{\mu}$ is decreased, it ends at the homoclinic explosion point $(\hat{\rho}_{\mathtt{r}}, 0)$. We also found the curve PD of period-doubling bifurcation that also emerges from $(\hat{\rho}_{\mathtt{r}}, 0)$ and ends at the corner $(1,1)$; it changes its criticality at a 1:2 resonance point R_2, from which a curve T of torus (Neimark–Sacker) bifurcation emerges for larger values of μ.

The background of Figure 1(a) is shaded by the kneading diagram of K_9, which distinguishes points of the $(\hat{\rho}, \hat{\mu})$-square symbolically in terms of the first nine 'excursions' of the positive branch $W^u_+(\mathbf{0})$ around either p^+ or p^-; see Section 2.1 for the definition. Changes in the kneading sequence are due to Shilnikov homoclinic bifurcations, and quite a few have been computed and are drawn as curves. Many of them begin at the homoclinic explosion point $(\hat{\rho}_{\mathtt{r}}, 0)$: some end at other points on the $\hat{\rho}$-axis, which are themselves homoclinic explosion points; others extend in $\hat{\mu}$ and reach the corner $(1,1)$; and yet others grow in $\hat{\mu}$ before returning to $(\hat{\rho}_{\mathtt{r}}, 0)$. The point $(\hat{\rho}^*, \hat{\mu}^*)$ in Figure 1(a) lies in a region where the shading by K_9 is intricate, which is visual evidence for the denseness of Shilnikov-type homoclinic bifurcations, a characteristic property of wild chaos. In white shades, we display additionally the regions in between consecutive curves of homoclinic bifurcation whose orbits have j excursions around p^+; these are seen to 'flatten' horizontally while steadily increasing in $\hat{\mu}$, providing evidence of the denseness of Shilnikov-type homoclinic bifurcations extending all the way to $\hat{\mu} = 1$ to the right of the torus bifurcation curve T. Note that the curves of homoclinic bifurcation above the curve $\mathrm{Hom}_{\mathtt{r}}$ are intrinsic to the four-dimensional system (1). They are not observable in the classic Lorenz system but, nevertheless, many of these curves end at the homoclinic explosion point $(\hat{\rho}_{\mathtt{r}}, 0)$. This demonstrates the role of this point as an organizing center of the dynamics of the extended system (1), beyond its relevance for the three-dimensional Lorenz system itself [31].

Building on these earlier results, we now turn to larger values of $\hat{\rho}$ or, equivalently, of ρ. Early work by Robbins [32] demonstrated the existence and stability of periodic orbits for $\rho \gg \sigma$ and described some of their bifurcations as ρ is decreased. Subsequently, Sparrow [34] summarized a sequence of bifurcations of periodic orbits that occur as ρ is decreased with σ and β fixed at their classic values; he also identified regions of periodic behaviour in parameter space. These insights were later extended by Dullin, Schmidt, Richter, and Grossmann [13], who studied the (ρ, σ)-parameter plane and provided a comprehensive view of the global bifurcation structure for larger values of both parameters. Further work by Barrio, Blesa, and Serrano [4] focused on global bifurcations at large ρ and computed maximal Lyapunov exponents to classify the nature of the existing attractors. Most recently, Ovsyannikov, Rademacher, Welter, and Lu [30] investigated periodic solutions in this large-ρ regime and provided a quantitative analysis via time averages, showing how these oscillations also appear in various extensions of the Lorenz model. These studies collectively establish the richness of the bifurcation structure associated with periodic orbits of the classic Lorenz system beyond its homoclinic bifurcations, which we continued as curves in earlier work [31].

In this paper, we perform a bifurcation study of how stable periodic orbits of the Lorenz system and their bifurcations extend for $\mu > 0$ and organize the bifurcation structure of system (1). Specifically, we consider two symmetric periodic orbits, which we refer to as Γ and Υ throughout; they are the periodic orbits in the "xy" and "x^2y^2" period-doubling windows identified in [34], and are attracting for $\mu = 0$ when (apprroximately) $\rho > 214.364$ and when $145 < \rho < 166$, respectively. Starting from the classic Lorenz system, we find and continue curves of bifurcations of Γ and Υ in the $(\hat{\rho}, \hat{\mu})$-square. For $\hat{\mu} = 0$ and decreasing $\hat{\rho}$, both these periodic orbits undergo symmetry-breaking bifurcations followed by period-doubling cascades to chaos — which is a classic route to chaos in three-dimensional flows. When these successive bifurcations are continued, they initially remain ordered in the same way as $\hat{\mu}$ increases. However, for sufficiently large $\hat{\mu}$ these bifurcation curves interact strongly, which involves criticality changes at certain codimension-two bifurcation points, and the emergence of curves of torus bifurcation. In particular, we find fold-flip bifurcation points, where one finds a simultaneous saddle-node and period-doubling bifurcation of a periodic orbit, which is a codimension-two bifurcation that requires a phase space of dimension at least four [23].

An overall picture emerges when we plot the bifurcation curves 'generated' by the periodic orbits Γ and Υ together with both the Lyapunov spectrum representing the dynamics of the one-dimensional unstable manifold $W^u(\mathbf{0})$, and the kneading diagram of K_9. Stable periodic orbits exist in strip-like periodic regions, which are the extensions of the corresponding periodic windows of the Lorenz system. In between, for low values of $\hat{\mu}$, one finds chaotic attractors generated by period-doubling cascades, with further, thinner periodic regions; here, the chaotic attractor is a quasiattractor. For sufficiently large $\hat{\mu}$, on the other hand, we find additional regions with pseudohyperbolic chaotic dynamics (as identified by the Lyapunov spectrum). In particular, curves of torus bifurcation near the boundary of these regions appear to be involved in the transition from a quasiattractor to a pseudohyperbolic chaotic attractor.

This paper is organized as follows. In Section 2 we describe some basic properties of system (1) and then introduce the kneading diagram and the compactification to the unit square. In Section 3 we introduce the basic symmetric, so called S-invariant periodic orbit Γ and present the structure of its bifurcations. In Section 4, we similarly study the S-invariant periodic orbit Υ. Section 5 then presents both bifurcation structures in the $(\hat{\rho},\hat{\mu})$-square overlaid onto the Lyapunov spectrum and the kneading diagram of K_9, respectively, as computed along the positive branch $W^u_+(\mathbf{0})$. Finally, in Section 6 we summarize the main findings and discuss directions for future research.

2 Background

System (1) is $\mathbb{Z}_2$-equivariant under the involution

$$\psi(x,y,z,w) = (-x,-y,z,w), \tag{2}$$

which is a rotation by π around the fixed-point subspace

$$\mathrm{Fix}(\psi) = \{(x,y,z,w) \in \mathbb{R}^4 \mid x = y = 0\}. \tag{3}$$

For $\rho > 1$, the system has three equilibria: the origin $\mathbf{0}$ and a symmetric pair $p^{\pm}$, related by ψ. For $\mu > 0$ and $\rho > 1$, the origin $\mathbf{0}$ has a one-dimensional unstable manifold $W^u(\mathbf{0})$ consisting of (the only) two trajectories that converge to $\mathbf{0}$ in backward time. Furthermore, $\mathbf{0}$ is a saddle-focus, so every homoclinic orbit to $\mathbf{0}$ is of Shilnikov type; since the saddle quantity of $\mathbf{0}$ is always positive, these are 'chaotic' Shilnikov homoclinic orbits [23]. We denote by $W^u_+(\mathbf{0})$ the branch of the unstable manifold that initially leaves $\mathbf{0}$ in the positive x-direction.

A notable feature of the classic Lorenz system for large values of ρ is that the periodic orbits listed in [34] have a specific type of symmetry or come in pairs. Namely, a periodic orbit $\Gamma \not\subset \mathrm{Fix}(\psi)$ with (minimal) period T is of one of two types [23]:

1. If Γ is mapped to itself as a set (not pointwise) under the symmetry transformation ψ, then ψ acts as the spatio-temporal symmetry $\psi(\Gamma)(t) = \Gamma(t+T/2)$, and Γ is called an *S-invariant* periodic orbit.
2. Otherwise, we refer to Γ as an *asymmetric* periodic orbit, and denote its symmetric counterpart by $\Gamma^* = \psi(\Gamma)$.

Because of this spatio-temporal symmetry, an S-invariant periodic orbit cannot undergo a period-doubling bifurcation [23]. However, pairs of asymmetric periodic orbits emerging from symmetry-breaking bifurcations do not have this restriction. Both types of periodic orbits play a central role in the bifurcation structure explored in this paper.

2.1 Kneading sequence and homoclinic orbits.

To find homoclinic bifurcations and then continue them as curves in the (ρ,μ)-plane, we follow the approach of [31] and compute the kneading diagram associated with $W^u_+(\mathbf{0})$. For each parameter pair $(\hat{\rho},\hat{\mu})$ on a sufficiently fine grid, the branch $W^u_+(\mathbf{0})$ is computed by integrating forward in time from a point near $\mathbf{0}$ along its unstable eigenvector; for this purpose we employ the Taylor-series integration method of the software package TIDES [1] with absolute and relative error tolerances of 10^{-16}. The kneading sequence records the successive excursions of $W^u_+(\mathbf{0})$ 'around' the equilibria $p^{\pm}$ and is defined as

$$S := (+s_1 s_2 \dots) \in \Sigma \subseteq \{+,-\}^{\mathbb{N}},$$

where $s_i = +$ if the ith extremum of x along $W^u_+(\mathbf{0})$ is a positive maximum, and $s_i = -$ if it is a negative minimum.

For visualization, each finite initial segment of S is mapped to the truncated kneading invariant

$$K_n = K_n(S) = \sum_{i=0}^{n} \frac{s_i}{2^{i+1}}, \qquad \text{for } S = (+s_1 s_2 \dots).$$

By construction, K_n partitions the interval $[0,1]$ into 2^n subintervals of length 2^{-n}, each corresponding to a distinct initial kneading sequence, to which we assign a specific color. Boundaries between regions of different color correspond to homoclinic bifurcations Hom_s with symbol sequences s; to avoid confusion with the kneading sequences at generic parameter points, we adopt the notation from [31] and represent in the symbol sequence s of a given homoclinic bifurcation excursions of $W^u_+(\mathbf{0})$ around the right equilibrium p^+ and the left equilibrium p^- by the letters `r` and `l`, respectively.

The kneading diagram provides an effective way of locating where in parameter space one expects to find particular homoclinic bifurcations. Based on such estimates, the corresponding Shilnikov homoclinic orbit can then be found accurately with Lin's method [27, 39, 22] as the solution of a suitably formulated boundary value problem; it is then readily continued as a curve in the (ρ,μ)-plane or the $(\hat{\rho},\hat{\mu})$-square. Throughout this paper, the continuation of equilibria, periodic orbits, and associated codimension-one bifurcation curves, including curves of homoclinic bifurcation, is performed with the continuation package AUTO [11, 12].

2.2 Parameter compactification to a square

To achieve an overall picture of the bifurcation structure, we introduce a compactification of the first quadrant of the (ρ,μ)-plane to the unit square; it is given by the transformation

$$\Phi(\rho,\mu) = (\hat{\rho},\hat{\mu}) := \left(\frac{\rho}{R+\sqrt{R^2+\rho^2}}, \frac{a\mu}{R+\sqrt{R^2+(a\mu)^2}} \right). \tag{4}$$

Here, we fix the parameters $R > 0$ and $a > 0$ to $R = 30$ and $a = 4$ so that the point (ρ^*,μ^*) is mapped to near the center of the unit square, at $(\hat{\rho}^*,\hat{\mu}^*) := \Phi(\rho^*,\mu^*) \approx (0.362, 0.394)$.

In the compactified $(\hat{\rho},\hat{\mu})$-square given by (4), the right boundary $\hat{\rho} = 1$ represents horizontal asymptotes in the limit $\rho \to \infty$ and the upper boundary $\hat{\mu} = 1$ vertical asymptotes in the limit $\mu \to \infty$. In contrast to the compactification to a quarter Poincaré disk, as we used in [31], the $(\hat{\rho},\hat{\mu})$-square of Figure 1(a) allows for the identification and continuation of previously undetected curves of homoclinic bifurcation near the organizing center 'at infinity', which is now at the corner point $(\hat{\rho},\hat{\mu}) = (1,1)$.

3 The basic S-invariant periodic orbit Γ

We first consider the attracting S-invariant periodic orbit Γ that exists and remains stable for all $\hat{\rho} > 0.870$ when $\hat{\mu} = 0$. This periodic orbit and its bifurcations have been studied in detail for the classic Lorenz system; see, for example, [34, 32, 29]. The periodic orbit Γ forms a single loop around p^+ and p^- before closing up and, for this reason, we refer to it as the *basic* S-invariant periodic orbit.

To set the stage, we consider $(\hat{\rho},\hat{\mu}) = (0.910, 0)$ for which Γ is the unique attractor of system (1); it is shown in projection onto the (x,y)-plane with the three saddle equilibria $\mathbf{0}$ and $p^{\pm}$ in Figure 2(a1), while panel (a2) shows these objects with the positive branch $W^u_+(\mathbf{0})$ of the unstable manifold of $\mathbf{0}$. Panel (a3) shows the time series in x of Γ; it features the invariance under a phase shift of half a period that is characteristic of S-invariant periodic orbits, and shows that Γ has the infinitely repeating kneading sequence $[+-]^\infty$. Panel (a4) shows the time series in x of $W^u_+(\mathbf{0})$, which is seen to converge to Γ after about five rotations around p^+ and p^-, as is represented by the kneading sequence $s = (+-+-+[+-]^\infty)$.

Panels (b1)–(b4) of Figure 2 show, in the same style, the pair of attracting asymmetric periodic orbits $\hat{\Gamma}$ and $\hat{\Gamma}^*$ at $(\hat{\rho},\hat{\mu}) = (0.890, 0)$, which are co-existing attractors of system (1); the basic periodic orbit Γ still exists and is shown in panel (b1), but is now of saddle type. Notice in panel (b2) that $W^u_+(\mathbf{0})$ now

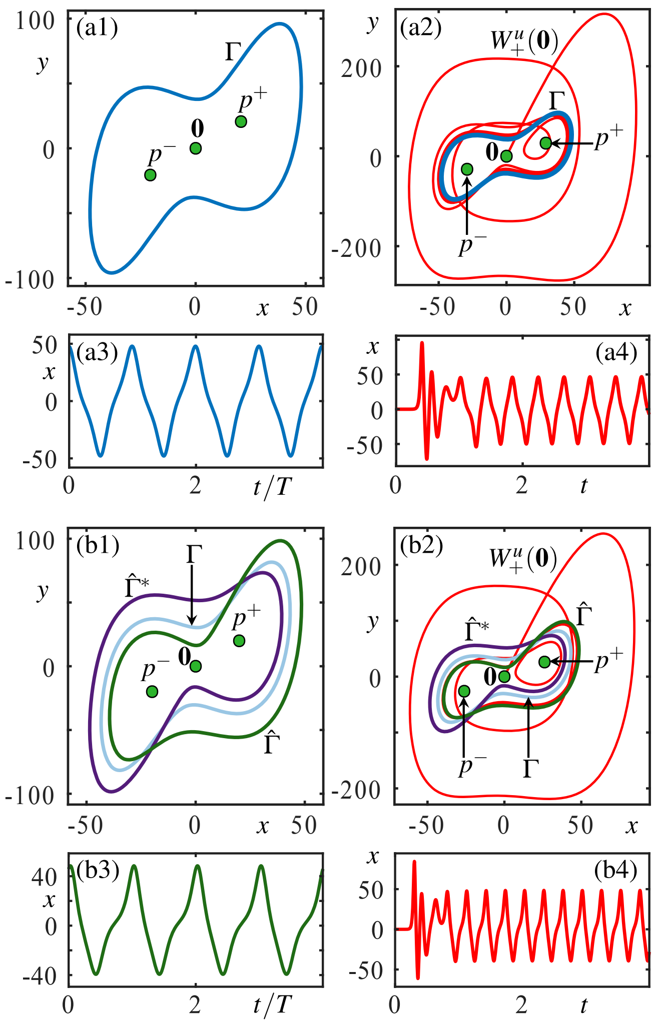

Figure 2: The basic S-invariant periodic orbit Γ (blue curve) and the branch $W^u_+(\mathbf{0})$ (red curve) are shown in panels (a1)–(a4) for $\hat{\rho} = 0.910$, when Γ is attracting; in panels (b1)–(b4) for $\hat{\rho} = 0.890$, they are shown when Γ is a saddle, together with the asymmetric periodic orbits $\hat{\Gamma}$ and $\hat{\Gamma}^*$ (green and purple curves); also shown are the three saddle equilibria $\mathbf{0}$ and $p^{\pm}$ (green dots). Panels (a1),(b1) and (a2),(b2) are projections onto the (x, y)-plane without and with $W^u_+(\mathbf{0})$, respectively; the time series in x of Γ is shown in panel (a3), that of $\hat{\Gamma}$ in panel (b3), and those of $W^u_+(\mathbf{0})$ in panels (a4),(b4).

accumulates on $\hat{\Gamma}$, implying that $\hat{\Gamma}^*$ is reached by the negative branch $W^u_-(\mathbf{0})$ (not shown). The time series in panel (b3) shows that $\hat{\Gamma}$ also has kneading sequence $[+-]^\infty$; however, it is not invariant under a phase shift of half a period, because the maxima are above $x = 40$, while the minima are not below $x = -40$. Panel (b4) reveals that $W^u_+(\mathbf{0})$ still has the same kneading sequence as in panel (a4). This is an important remark because it shows that Γ, $\hat{\Gamma}$, and $\hat{\Gamma}^*$ all exist in a region with the same kneading invariant. Consequently, thesymmetry-breaking bifurcation from an S-invariant to asymmetric periodic orbits is not detected by the kneading diagram.

3.1 Bifurcations of Γ

We now investigate the bifurcations of the S-invariant periodic orbit Γ from Figure 2(a1) as the parameter $\hat{\rho}$ is varied. The results are presented in Figure 3, which shows two one-parameter bifurcation diagrams for the fixed values $\hat{\mu} = 0$ and $\hat{\mu} = 0.2$, each with two rows. The top row displays the branches of periodic orbits in terms of their periods, where we plot half the period along 'period-doubled' branches, so they connect at period-doubling bifurcation points. The bottom row shows the maximum of x along the periodic orbits,

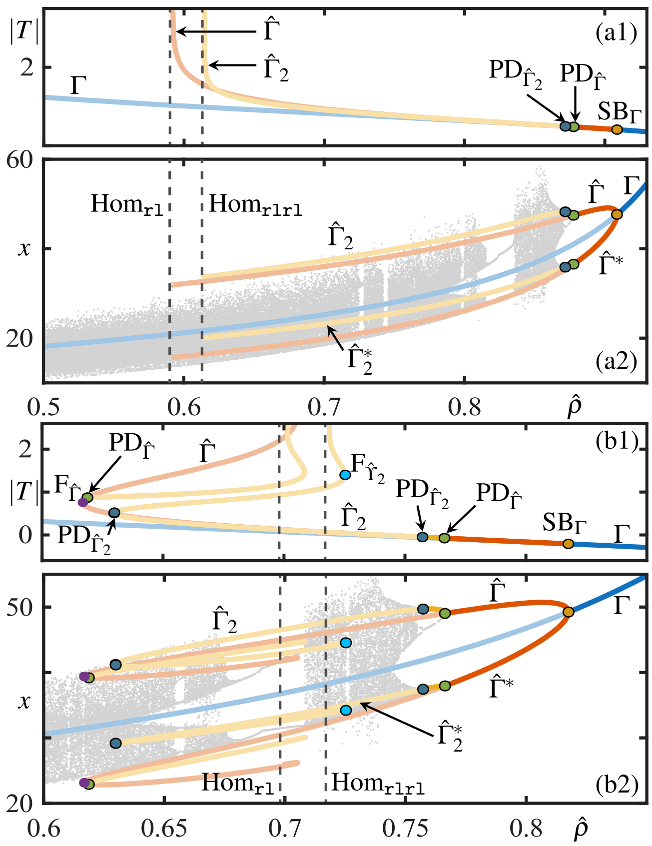

Figure 3: One-parameter bifurcation diagrams in $\hat{\rho}$ for $\hat{\mu} = 0$ (a), and $\hat{\mu} = 0.2$ (b), shown in terms of the period $|T|$ in panels (a1),(b1) and the maximum of x in panels (a2),(b2). Shown are branches of Γ (dark blue when attracting, light blue when a saddle), $\hat{\Gamma}$, $\hat{\Gamma}^*$ (dark red when attracting, light red when saddles), and $\hat{\Gamma}_2$, $\hat{\Gamma}_2^*$, (dark orange when attracting, light yellow when saddles); also shown are points SB_Γ of symmetry-breaking (orange), $\mathrm{PD}_{\hat{\Gamma}}$ (green) and $\mathrm{PD}_{\hat{\Gamma}_2}$ (dark blue) of period-doubling, and $\mathrm{F}_{\hat{\Gamma}}$ (purple) and $\mathrm{F}_{\hat{\Gamma}_2}$ (cyan) of fold bifurcation. In the background of panels (a2),(b2) is the orbit diagram (grey points) of the local maxima of x of the attractor at each parameter value.

overlayed on the orbit diagram of the corresponding attractor of system (1) at each $\hat{\rho}$-value, which provides additional insight into the global dynamics of the system. Here, we use bright and pastel colors to indicate the stability of the periodic orbits: attracting ones are bright and those of saddle type are shown in pastel shades.

The pair of asymmetric periodic orbits $\hat{\Gamma}$ and $\hat{\Gamma}^*$, bifurcating from the family of S-invariant periodic orbits Γ, undergo bifurcations themselves: we found symmetry-breaking, period-doubling, and fold bifurcations. In Figure 3, the periodic orbit involved in the bifurcation is indicated by the subscript. This notation is helpful, here and in later sections, when more periodic orbits and their bifurcations are considered. Observe in Figure 3 that the branches labeled $\hat{\Gamma}$ and $\hat{\Gamma}_2$ end on homoclinic orbits which are marked by vertical dashed lines.

The attractors displayed in the background were found by using a standard parameter-sweeping technique: for each $\hat{\rho}$-value, a long integration is performed, the initial transient is discarded, and the last 100 local maxima of x are then recorded; for every increment of $\hat{\rho}$, the final point of the previous simulation (which is assumed to be close to the next attractor) is used as the new initial condition. In order to capture potential multistability in the system, this process is carried out again for decreasing values of $\hat{\rho}$ by starting from a large value.

The starting point in Figure 3(a) is the case $\hat{\mu} = 0$ of the classic Lorenz system. We begin the continuation from the attracting S-invariant periodic orbit Γ at $\hat{\rho} = 0.910$, shown in Figure 2(a). It exists on the right-hand side of panels (a1) and (a2) and remains attracting for all $\hat{\rho} > 0.910$. As $\hat{\rho}$ is decreased, Γ loses stability in the supercritical symmetry-breaking bifurcation SB_Γ at $\hat{\rho} \approx 0.909$, and subsequently disappears in the homoclinic bifurcation $\mathrm{Hom}_{\mathtt{r}}$ at $\hat{\rho} \approx 0.221$ (not shown, since outside the shown range). The bifurcation SB_Γ gives rise to the pair $\hat{\Gamma}$ and $\hat{\Gamma}^*$ of attracting asymmetric periodic orbits from Figure 2(b1). Both branches of $\hat{\Gamma}$ and $\hat{\Gamma}^*$ are shown in Figure 3(a2). This pair undergoes a supercritical period-doubling bifurcation $\mathrm{PD}_{\hat{\Gamma}}$ at $\hat{\rho} \approx 0.878$, after which the family is unstable and ultimately ends at the homoclinic bifurcation $\mathrm{Hom}_{\mathtt{rl}}$ at $\hat{\rho} \approx 0.592$; as shown in panel (a1), observe that the period of $\hat{\Gamma}$ goes to infinity at this $\hat{\rho}$-value.

At $\mathrm{PD}_{\hat{\Gamma}}$, the pair $\hat{\Gamma}_2$ and $\hat{\Gamma}_2^*$ of attracting asymmetric periodic orbits is created, each with approximately twice the period of $\hat{\Gamma}$ and $\hat{\Gamma}^*$. The two respective branches have the same period and coincide in Figure 3(a1), but are distinguished in panel (a2). This pair loses stability in the supercritical period-doubling bifurcation $\mathrm{PD}_{\hat{\Gamma}_2}$ at $\hat{\rho} \approx 0.872$ and ceases to exist at the homoclinic bifurcation $\mathrm{Hom}_{\mathtt{rlrl}}$ at $\hat{\rho} \approx 0.615$, as seen in panel (a1). For decreasing $\hat{\rho}$ just past $\mathrm{PD}_{\hat{\Gamma}_2}$, a period-doubling cascade gives rise to a pair of chaotic attractors near $\hat{\rho} \approx 0.870$, as is illustrated by the orbit diagram in the background of panel (a2).

Figure 3(b) shows the bifurcation diagram for $\hat{\mu} = 0.2$, with notable differences compared to $\hat{\mu} = 0$; in particular, the homoclinic bifurcations are now of Shilnikov type. However, here as well, the attracting periodic orbit Γ, on the right-hand side of panels (b1) and (b2), remains attracting for all $\hat{\rho} > 0.818$. As $\hat{\rho}$ is decreased, Γ again loses stability in the supercritical symmetry-breaking bifurcation SB_Γ, now at $\hat{\rho} \approx 0.818$. It then disappears at the Shilnikov homoclinic bifurcation $\mathrm{Hom}_{\mathtt{r}}$ at $\hat{\rho} \approx 0.303$ (not shown, since outside the shown range).

The pair of attracting asymmetric periodic orbits $\hat{\Gamma}$ and $\hat{\Gamma}^*$ is created at SB_Γ and loses stability at the supercritical period-doubling bifurcation $\mathrm{PD}_{\hat{\Gamma}}$ at $\hat{\rho} \approx 0.767$. Note how both branches $\hat{\Gamma}$ and $\hat{\Gamma}^*$ approach the (Shilnikov) homoclinic bifurcation $\mathrm{Hom}_{\mathtt{rl}}$ at $\hat{\rho} \approx 0.700$ in a characteristic *snaking* or spiraling fashion [23] in panels (b1) and (b2), respectively. In the process, these periodic orbits undergo a sequence of fold bifurcations. In Figure 3(b), we label only the first of these, namely, $\mathrm{F}_{\hat{\Gamma}}$ at $\hat{\rho} \approx 0.617$. Past $\mathrm{F}_{\hat{\Gamma}}$, the periodic orbits $\hat{\Gamma}$ and $\hat{\Gamma}^*$ undergo, in addition, infinitely many period-doubling bifurcations with alternating criticality. Specifically, we labeled the first such subcritical period-doubling bifurcation as $\mathrm{PD}_{\hat{\Gamma}}$, which lies at $\hat{\rho} \approx 0.619$.

Figure 3(b) also shows the branches of periodic orbits that bifurcate from the two period-doubling bifurcations $\mathrm{PD}_{\hat{\Gamma}}$. As panel (b1) illustrates, these branches do not connect to each other. We label only the branches $\hat{\Gamma}_2$ and $\hat{\Gamma}_2^*$ of the asymmetric periodic orbits originating from the right-most, supercritical bifurcation $\mathrm{PD}_{\hat{\Gamma}}$. Similar to the corresponding branches in Figure 3(a), they are involved in a period-doubling cascade that gives rise to a pair of chaotic attractors. In contrast to panel (a), however, the chaotic behaviour occurs for lower values of $\hat{\rho}$; note the difference in range of $\hat{\rho}$ for the background orbit diagrams in panels (a2) and (b2).

The two branches of periodic orbits that emerge from the period-doubling bifurcations $\mathrm{PD}_{\hat{\Gamma}}$ also undergo additional fold bifurcations and further period-doubling bifurcations with alternating criticalities, while approaching yet other homoclinic bifurcations. In panel (b), we show and label only those along the branches $\hat{\Gamma}_2$ and $\hat{\Gamma}_2^*$; namely, the first two period-doubling bifurcations, both labeled $\mathrm{PD}_{\hat{\Gamma}_2}$, one supercritical at $\hat{\rho} \approx 0.757$ and the other subcritical at $\hat{\rho} \approx 0.630$. These occur before the first two fold bifurcations, both labeled $\mathrm{F}_{\hat{\Gamma}_2}$, at $\hat{\rho} \approx 0.725$ and $\hat{\rho} \approx 0.630$. Note that, on the scale of Figure 3(b), it is difficult to distinguish the fold bifurcation $\mathrm{F}_{\hat{\Gamma}_2}$, which lies to the left of the period-doubling bifurcation $\mathrm{PD}_{\hat{\Gamma}_2}$ at almost the same $\hat{\rho}$-value.

3.2 Two-parameter bifurcation diagram of Γ

Figure 4 shows the two-parameter bifurcation diagram of system (1) in the $(\hat{\rho}, \hat{\mu})$-square. Plotted are the codimension-one bifurcation curves SB_Γ of symmetry-breaking bifurcation, $\mathrm{PD}_{\hat{\Gamma}}$ and $\mathrm{PD}_{\hat{\Gamma}_2}$ of period-doubling bifurcation, and $\mathrm{F}_{\hat{\Gamma}}$ and $\mathrm{F}_{\hat{\Gamma}_2}$ of fold bifurcation of periodic orbits. These curves were continued with AUTO by starting from the respective bifurcation points identified in Figure 3. Also shown are the

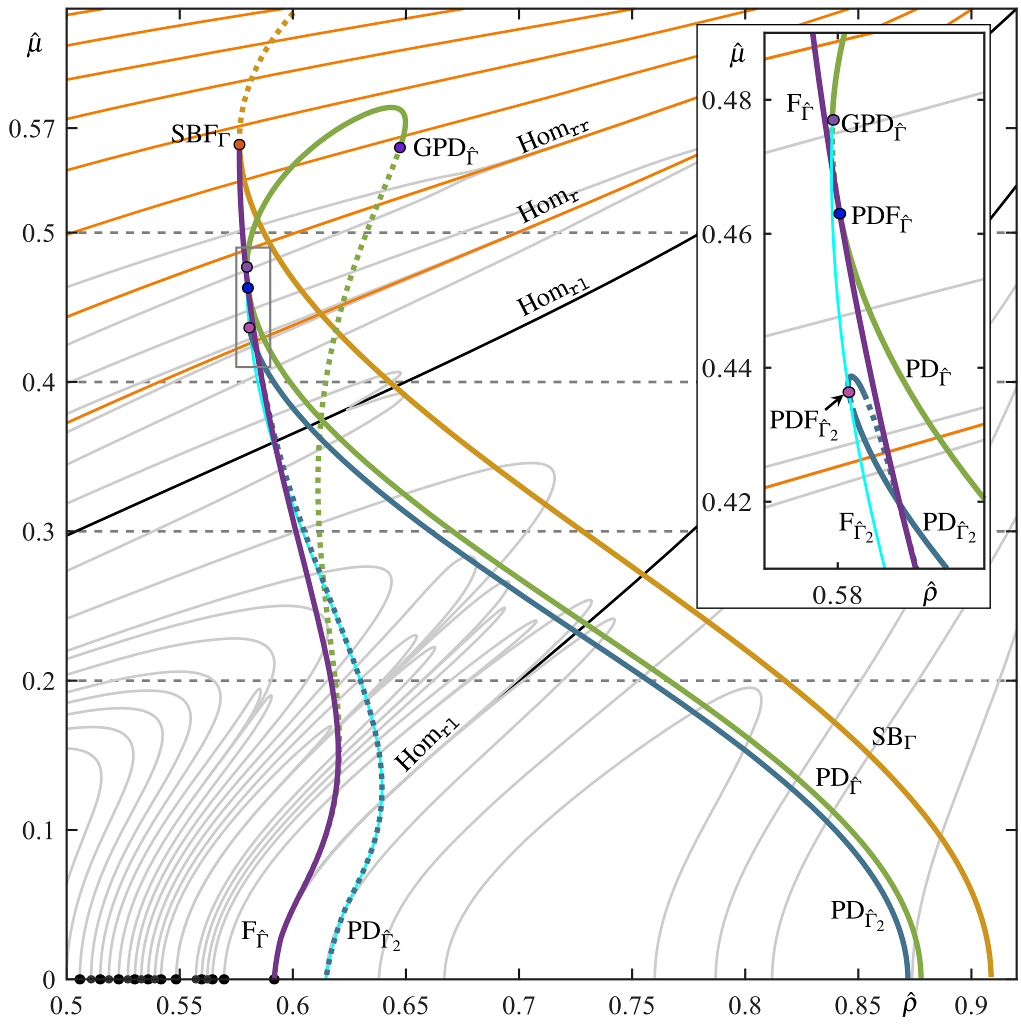

Figure 4: Two-parameter bifurcation diagram in the $(\hat{\rho}, \hat{\mu})$-square with bifurcation curves associated with Γ; shown are the curves SB_Γ (yellow solid segments when supercritical, dashed segments when subcritical) of symmetry-breaking, $\mathrm{PD}_{\hat{\Gamma}}$ (green) and $\mathrm{PD}_{\hat{\Gamma}_2}$ (blue) of period-doubling, and $\mathrm{F}_{\hat{\Gamma}}$ (purple) and $\mathrm{F}_{\hat{\Gamma}_2}$ (cyan) of folds of periodic orbits bifurcation, together with the codimension-two points of symmetry-breaking-fold SBF_Γ, fold-flip $\mathrm{PDF}_{\hat{\Gamma}}$ and $\mathrm{PDF}_{\hat{\Gamma}_2}$, and generalized period-doubling bifurcation $\mathrm{GPD}_{\hat{\Gamma}}$. The background shows curves of secondary homoclinic bifurcations. The horizontal dashed line at $\hat{\mu} = 0.2$ corresponds to Figure 3(b), and those at $\hat{\mu} = 0.3$, 0.5, and 0.57 to the one-parameter bifurcation diagrams in Figure 6. The inset provides an enlargement near the codimension-two points $\mathrm{PDF}_{\hat{\Gamma}}$, $\mathrm{PDF}_{\hat{\Gamma}_2}$, and $\mathrm{GPD}_{\hat{\Gamma}}$, where solid segments represent a supercritical and dashed ones a subcritical bifurcation.

codimension-two bifurcation points $\mathrm{PDF}_{\hat{\Gamma}}$ and $\mathrm{PDF}_{\hat{\Gamma}_2}$ of *fold-flip* bifurcation, $\mathrm{GPD}_{\hat{\Gamma}}$ of *generalized period-doubling* bifurcation, and SBF_Γ of *symmetry-breaking–fold* bifurcation [23]. These curves are overlaid on the curves of secondary homoclinic bifurcations from Figure 1. The horizontal dashed line at $\hat{\mu} = 0.2$ in Figure 4 corresponds to Figure 3(b); one-parameter bifurcation diagrams along the dashed lines at $\hat{\mu} = 0.3$, 0.5, and 0.57 will be discussed below. The inset of Figure 4 provides an enlargement of the bifurcation diagram near the codimension-two points $\mathrm{PDF}_{\hat{\Gamma}}$, $\mathrm{PDF}_{\hat{\Gamma}_2}$, and $\mathrm{GPD}_{\hat{\Gamma}}$.

The curve SB_Γ of symmetry-breaking bifurcation in Figure 4 emanates from the $\hat{\rho}$-axis at $\hat{\rho} \approx 0.909$ and extend beyond this figure until it ends at the point $(\hat{\rho}, \hat{\mu}) = (1, 1)$. To the right of SB_Γ, the basic S-invariant periodic orbit Γ is attracting and the sole attractor of system (1), whereas to its left, Γ is a saddle periodic orbit. Along SB_Γ, there is one change of criticality, namely, at the codimension-two point $(\hat{\rho}, \hat{\mu}) \approx (0.576, 0.559)$, labeled SBF_Γ. For $\hat{\mu} < 0.559$, the symmetry-breaking bifurcation is supercritical,

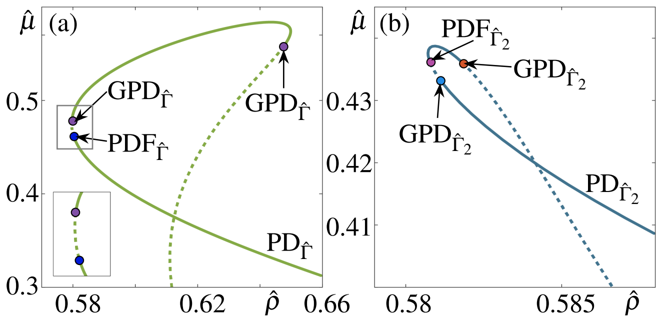

Figure 5: Supercritical (solid) and subcritical (dashed) segments of the period-doubling curves $\mathrm{PD}_{\hat{\Gamma}}$ in panel (a) and $\mathrm{PD}_{\hat{\Gamma}_2}$ in panel (b), with bounding codimension-two points $\mathrm{PDF}_{\hat{\Gamma}}$ and $\mathrm{PDF}_{\hat{\Gamma}_2}$ of fold-flip, and $\mathrm{GPD}_{\hat{\Gamma}}$ and $\mathrm{GPD}_{\hat{\Gamma}_2}$ of generalized period-doubling bifurcation.

so the bifurcating periodic orbits $\hat{\Gamma}$ and $\hat{\Gamma}^*$ are attracting. For $\hat{\mu} > 0.559$, the symmetry-breaking bifurcation is subcritical, and a pair of asymmetric saddle-type periodic orbits $\hat{\Gamma}$ and $\hat{\Gamma}^*$ emenates from SB_Γ in the direction of increasing $\hat{\rho}$. As expected, a curve of fold bifurcations emanates from SBF_Γ, which is tangent to SB_Γ; this is the fold bifurcation $\mathrm{F}_{\hat{\Gamma}}$ of $\hat{\Gamma}$ and $\hat{\Gamma}^*$ from Figure 3(b). For decreasing $\hat{\mu}$, the curve $\mathrm{F}_{\hat{\Gamma}}$ is tangent to and ends at the homoclinic bifurcation $\mathrm{Hom}_{\mathtt{r1}}$ at $(\hat{\rho}, \hat{\mu}) \approx (0.592, 0)$.

The curves $\mathrm{PD}_{\hat{\Gamma}}$ and $\mathrm{PD}_{\hat{\Gamma}_2}$ of period-doubling bifurcation in Figure 4 were continued from the points $\mathrm{PD}_{\hat{\Gamma}}$ at $\hat{\rho} \approx 0.878$ and $\mathrm{PD}_{\hat{\Gamma}_2}$ at $\hat{\rho} \approx 0.872$ in Figure 3(a) for $\hat{\mu} = 0$. As $\hat{\mu}$ is increased, the curve $\mathrm{PD}_{\hat{\Gamma}}$ reaches a maximum at $(\hat{\rho}, \hat{\mu}) \approx (0.643, 0.584)$ and then returns to the $\hat{\rho}$-axis at $\hat{\rho} \approx 0.592$, forming an arc with a single point of self-intersection. Similarly, the curve $\mathrm{PD}_{\hat{\Gamma}_2}$ grows for increasing $\hat{\mu}$, reaches a maximum at $(\hat{\rho}, \hat{\mu}) \approx (0.581, 0.439)$, and returns to the $\hat{\rho}$-axis to the right of the curve $\mathrm{PD}_{\hat{\Gamma}}$ at $\hat{\rho} \approx 0.615$. This curve also forms an arc with a single self-intersection, which is barely visible at the scale of Figure 4; an enlargement near this point of self-intersection is shown in the inset. Note that the endpoints of the curves $\mathrm{PD}_{\hat{\Gamma}}$ and $\mathrm{PD}_{\hat{\Gamma}_2}$ on the $\hat{\rho}$-axis coincide with those of the secondary homoclinic bifurcation curves $\mathrm{Hom}_{\mathtt{r1}}$ and $\mathrm{Hom}_{\mathtt{r1r1}}$, respectively.

Because the curves $\mathrm{PD}_{\hat{\Gamma}}$ and $\mathrm{PD}_{\hat{\Gamma}_2}$ have points of self intersection, there must be degenerate period-doubling points on both curves. For $\mathrm{PD}_{\hat{\Gamma}}$, we found the fold-flip point $\mathrm{PDF}_{\hat{\Gamma}}$ at $(\hat{\rho}, \hat{\mu}) \approx (0.580, 0.463)$, where the curve $\mathrm{PD}_{\hat{\Gamma}}$ is tangent to the fold curve $\mathrm{F}_{\hat{\Gamma}}$ of $\hat{\Gamma}$, and two generalized period-doubling points $\mathrm{GPD}_{\hat{\Gamma}}$ at $(\hat{\rho}, \hat{\mu}) \approx (0.647, 0.557)$ and $(\hat{\rho}, \hat{\mu}) \approx (0.580, 0.477)$. The bifurcation $\mathrm{PD}_{\hat{\Gamma}}$ is supercritical from $(\hat{\rho}, \hat{\mu}) \approx (0.878, 0)$ up to the point $\mathrm{PDF}_{\hat{\Gamma}}$ and between the two points $\mathrm{GPD}_{\hat{\Gamma}}$, and subcritical otherwise; this is illustrated in Figure 5(a). At the fold-flip bifurcation $\mathrm{PDF}_{\hat{\Gamma}}$ there is simultaneous saddle-node and period-doubling bifurcation of $\hat{\Gamma}$; additional bifurcation curves that exist near $\mathrm{PDF}_{\hat{\Gamma}}$ are not shown here. At the two points $\mathrm{GPD}_{\hat{\Gamma}}$, the third-order coefficient of the period-doubling normal form is zero; as a result, a saddle-node bifurcation of the period-doubled periodic orbit $\hat{\Gamma}_2$ emerges from this codimension-two point. Figure 4 shows only the branch $\mathrm{F}_{\hat{\Gamma}_2}$ enlarged in the inset that emanates from the left-most point $\mathrm{F}_{\hat{\Gamma}_2}$ in Figure 3(b). For decreasing $\hat{\mu}$, the curve $\mathrm{F}_{\hat{\Gamma}_2}$ converges to the homoclinic bifurcation point $\mathrm{Hom}_{\mathtt{r1r1}}$ at $(\hat{\rho}, \hat{\mu}) \approx (0.615, 0)$.

A similar scenario occurs along the curve $\mathrm{PD}_{\hat{\Gamma}_2}$. The inset of Figure 4 shows the fold-flip bifurcation point $\mathrm{PDF}_{\hat{\Gamma}_2}$ at $(\hat{\rho}, \hat{\mu}) \approx (0.581, 0.436)$, where the curve $\mathrm{F}_{\hat{\Gamma}_2}$ is tangent to $\mathrm{PD}_{\hat{\Gamma}_2}$ and the criticality of $\mathrm{PD}_{\hat{\Gamma}_2}$ changes. In addition, there are two generalized period-doubling points $\mathrm{GPD}_{\hat{\Gamma}_2}$ on $\mathrm{PD}_{\hat{\Gamma}_2}$, namely, at $(\hat{\rho}, \hat{\mu}) \approx (0.581, 0.433)$ and $(\hat{\rho}, \hat{\mu}) \approx (0.582, 0.436)$. These points are not shown in Figure 4, but their role in criticality changes along $\mathrm{PD}_{\hat{\Gamma}_2}$ is illustrated in Figure 5(b). The period-doubling bifurcation $\mathrm{PD}_{\hat{\Gamma}_2}$ is supercritical from $(\hat{\rho}, \hat{\mu}) \approx (0.872, 0)$ up to the left point $\mathrm{GPD}_{\hat{\Gamma}_2}$, and again between the point $\mathrm{PDF}_{\hat{\Gamma}_2}$ and the right point $\mathrm{GPD}_{\hat{\Gamma}_2}$; it is subcritical otherwise. Note the different relative order of the points $\mathrm{PDF}_{\hat{\Gamma}_2}$ and $\mathrm{GPD}_{\hat{\Gamma}_2}$ on $\mathrm{PD}_{\hat{\Gamma}_2}$ in comparison with those on $\mathrm{PD}_{\hat{\Gamma}}$; compare panels (a) and (b) of Figure 5.

We further illustrate the transitions and criticality changes seen in Figures 4 and 5 with three one-parameter bifurcation diagrams of the basic S-invariant periodic orbit Γ. Figure 6 presents, in the layout of Figure 3, those for $\hat{\mu} = 0.3$, $\hat{\mu} = 0.5$, and $\hat{\mu} = 0.57$, along the corresponding horizontal lines in Figure 4.

Figure 6(a) shows the case $\hat{\mu} = 0.3$. The branches of Γ and $\hat{\Gamma}$ have a bifurcation structure that is similar

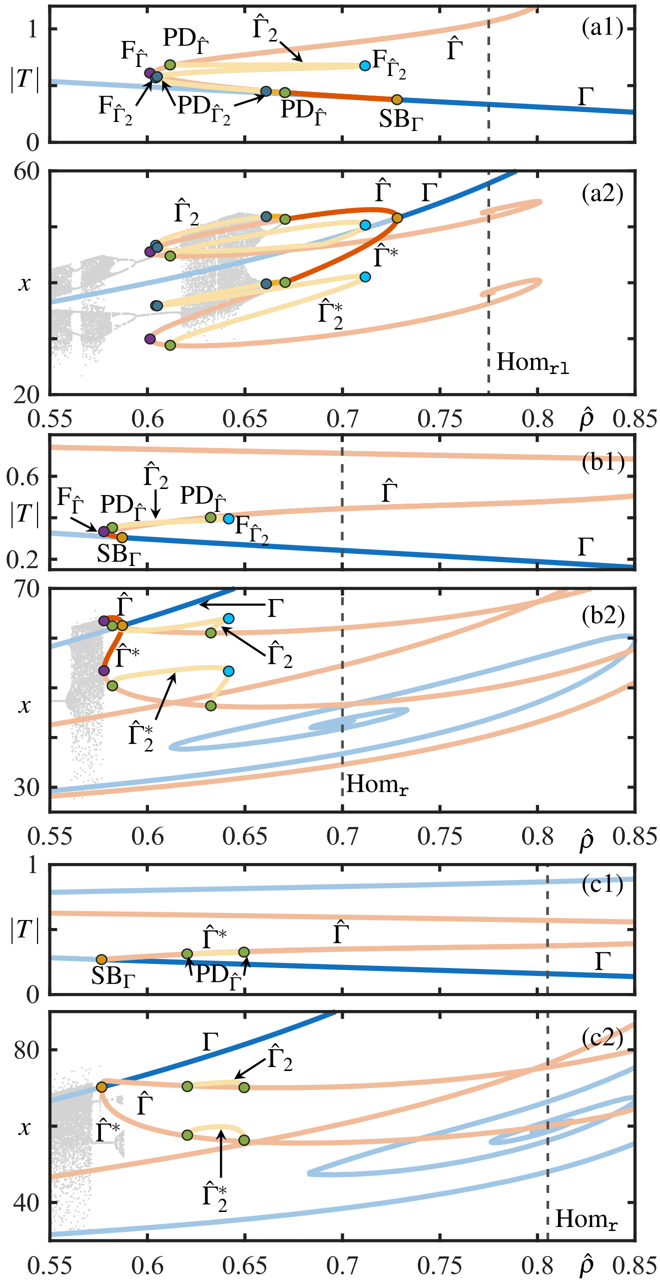

Figure 6: One-parameter bifurcation diagrams in $\hat{\rho}$ for $\hat{\mu} = 0.3$ (a), $\hat{\mu} = 0.5$ (b), and $\hat{\mu} = 0.57$ (c), showing branches of Γ, $\hat{\Gamma}$, $\hat{\Gamma}^*$, $\hat{\Gamma}_2$, $\hat{\Gamma}_2^*$, overlaid on the orbit diagram; compare with Figure 3.

to that for $\hat{\mu} = 0.2$ in Figure 3(b1). A key difference in Figure 6(a) is that the branches $\hat{\Gamma}_2$ and $\hat{\Gamma}_2^*$ of periodic orbits, which emanate from the supercritical period-doubling bifurcation $\mathrm{PD}_{\hat{\Gamma}}$ at $\hat{\rho} \approx 0.670$ reconnect with $\hat{\Gamma}$ at the subcritical bifurcation point $\mathrm{PD}_{\hat{\Gamma}}$ at $\hat{\rho} \approx 0.612$; compare with Figure 3(b1), where they approach $\mathrm{Hom}_{\mathtt{r1r1}}$ instead. In other words, as $\hat{\mu}$ is increased from 0.2 to 0.3, two separate branches of periodic orbits have connected in a saddle transition. Such merging or splitting of branches is typical for periodic orbits near Shilnikov-type homoclinic bifurcations [23]; moreover, this change is consistent with the fact that the secondary homoclinic curve $\mathrm{Hom}_{\mathtt{r1r1}}$ reaches its maximum below $\hat{\mu} = 0.3$; see Figure 4. As for $\hat{\mu} = 0$ and $\hat{\mu} = 0.2$, a period-doubling cascade starting from the supercritical bifurcation point $\mathrm{PD}_{\hat{\Gamma}}$ gives rise to a pair of chaotic attractors just below $\hat{\rho} \approx 0.659$, as seen in Figure 6(b2).

Figure 6(b) shows the case $\hat{\mu} = 0.5$. As $\hat{\rho}$ is decreased, the attracting periodic orbit Γ on the right of panel (b1) loses stability in the supercritical symmetry-breaking bifurcation SB_{Γ}, now at $\hat{\rho} \approx 0.587$; it then leaves the frame to the left, undergoes a fold bifurcation (not shown), and then re-enter the frame of panel (b2), where it is seen to end at the homoclinic bifurcation $\mathrm{Hom}_{\mathtt{r}}$ at $\hat{\rho} \approx 0.699$ in the typical spiraling fashion. Unlike in earlier cases, the families of asymmetric periodic orbits $\hat{\Gamma}$ and $\hat{\Gamma}^*$ emanating from SB_Γ lose stability at the fold bifurcation $\mathrm{F}_{\hat{\Gamma}}$ at $\hat{\rho} \approx 0.578$. These branches do not end in homoclinic bifurcations but reconnect with Γ at another symmetry-breaking bifurcation outside the frame. Also shown on the branches of $\hat{\Gamma}$ and $\hat{\Gamma}^*$ is a pair of bifurcation points $\mathrm{PD}_{\hat{\Gamma}}$ of opposite criticality. As in Figure 6(a), the periodic orbits $\hat{\Gamma}_2$ and $\hat{\Gamma}_2^*$ are created at one of these points and reconnect at the other. We found no further period-doubling bifurcations on $\hat{\Gamma}_2$ or $\hat{\Gamma}_2^*$. Figure 3(b2) shows that $\mathrm{F}_{\hat{\Gamma}}$ lies right at the onset of chaotic dynamics, which suggests that it is (more globally) involved in creating a boundary crisis of a chaotic attractor.

Finally, Figure 6(c) shows the one-parameter bifurcation diagram for $\hat{\mu} = 0.57$. The sequence of bifurcations is similar to panel (b): the basic periodic orbit Γ loses stability at SB_Γ for $\hat{\rho} \approx 0.577$, which is now subcritical, before disappearing at $\mathrm{Hom}_{\mathtt{r}}$ for $\hat{\rho} \approx 0.804$. In agreement with Figure 4, the point SB_Γ now gives rise to a pair of asymmetric saddle periodic orbits $\hat{\Gamma}$ and $\hat{\Gamma}^*$, which exist to its right. As a consequence, the fold bifurcation $\mathrm{F}_{\hat{\Gamma}}$ no longer occurs and, consequently, can no longer be associated with the (dis)appearance of the chaotic attractor that still emerges to the left of SB_Γ.

4 The S-invariant periodic orbit Υ

We now focus on the other S-invariant periodic orbit Υ, which also exists for the classic Lorenz system. Unlike the basic periodic orbit Γ, it is attracting only within a bounded periodic window in parameter space. In the classic Lorenz system, this window was identified in [34] as the x^2y^2 period-doubling window, and it corresponds to $0.814 < \hat{\rho} < 0.836$ after compactification. The notation x^2y^2 of [34] reflects the topological structure of Υ when projected onto the (x,y)-plane, which is encoded here by the infinitely repeating kneading sequence $(++--)^\infty$.

Figure 7 illustrates, in the style of Figure 2, the attracting S-invariant periodic orbit Υ at $(\hat{\rho},\hat{\mu}) = (0.830,0)$ in panels (a), where it is the only attractor of system (1), and at $(\hat{\rho},\hat{\mu}) = (0.820,0)$ in panels (b), where it is of saddle type and coexists with the bifurcating pair $\hat{\Upsilon}$ and $\hat{\Upsilon}^*$ of attracting asymmetric periodic orbits. Panel (a2) shows that the branch $W^u_+(\mathbf{0})$ accumulates on Υ after looping six times around p^+ and p^-. The (infinite) kneading sequence at this parameter value is $s = (+-+---(++--)^\infty)$, where $(++--)^\infty$ indicates convergence to Υ, as is illustrated by the time series of x in panel (a4).

Figure 7(b1) shows the now saddle periodic orbit Υ at $(\hat{\rho},\hat{\mu}) = (0.820,0)$ with the pair of attracting asymmetric periodic orbits $\hat{\Upsilon}$ and $\hat{\Upsilon}^*$. Notice in panel (b2) that $W^u_+(\mathbf{0})$ accumulates on $\hat{\Upsilon}$, implying that $\hat{\Upsilon}^*$ is reached by the negative branch $W^u_-(\mathbf{0})$ (not shown). Panel (b4) shows that $W^u_+(\mathbf{0})$ has a different kneading sequence here than for $\hat{\rho} \approx 0.830$; compare with panel (a4).

4.1 Bifurcations of Υ

Figure 8 shows two one-parameter bifurcation diagrams of the S-invariant periodic orbit Υ, presented in the style of Figures 3 and 6. Figure 8(a) for $\hat{\mu} = 0$ is the case of the classic Lorenz system; the continuations were started from the attracting S-invariant periodic orbit Υ at $\hat{\rho} = 0.830$ from Figure 7(a1). For increasing $\hat{\rho}$, the periodic orbit Υ collides with its saddle-type counterpart and disappears at the fold bifurcation F_Υ at $\hat{\rho} \approx 0.836$. Just past F_Υ in Figure 8(a), a chaotic attractor is created, meaning that F_Υ constitutes the end point of a periodic window. For decreasing values of $\hat{\rho}$, the saddle branch of Υ ends at the homoclinic bifurcation $\mathrm{Hom}_{\mathtt{rl}}$ at $\hat{\rho} \approx 0.592$. For the (initially) attracting branch, the bifurcation structure in Figure 8(a) closely resembles that of Γ in Figure 3(a): Υ first loses stability in a supercritical symmetry-breaking bifurcation SB_Υ at $\hat{\rho} \approx 0.824$, and then disappears in the homoclinic bifurcation $\mathrm{Hom}_{\mathtt{r}}$ at $\hat{\rho} \approx 0.221$ (not shown, since outside the range).

The bifurcation SB_Υ gives rise to the pair of attracting asymmetric periodic orbits $\hat{\Upsilon}$ and $\hat{\Upsilon}^*$ shown in Figure 7(b1); both branches are also visible in Figure 8(a2). This pair loses stability at the supercritical period-doubling bifurcation $\mathrm{PD}_{\hat{\Upsilon}}$ at $\hat{\rho} \approx 0.818$ and, subsequently, disappears in the homoclinic bifurcation $\mathrm{Hom}_{\mathtt{rllr}}$ at $\hat{\rho} \approx 0.570$. At $\mathrm{PD}_{\hat{\Upsilon}}$, period-doubled attracting periodic orbits $\hat{\Upsilon}_2$ and $\hat{\Upsilon}_2^*$ are created. Both

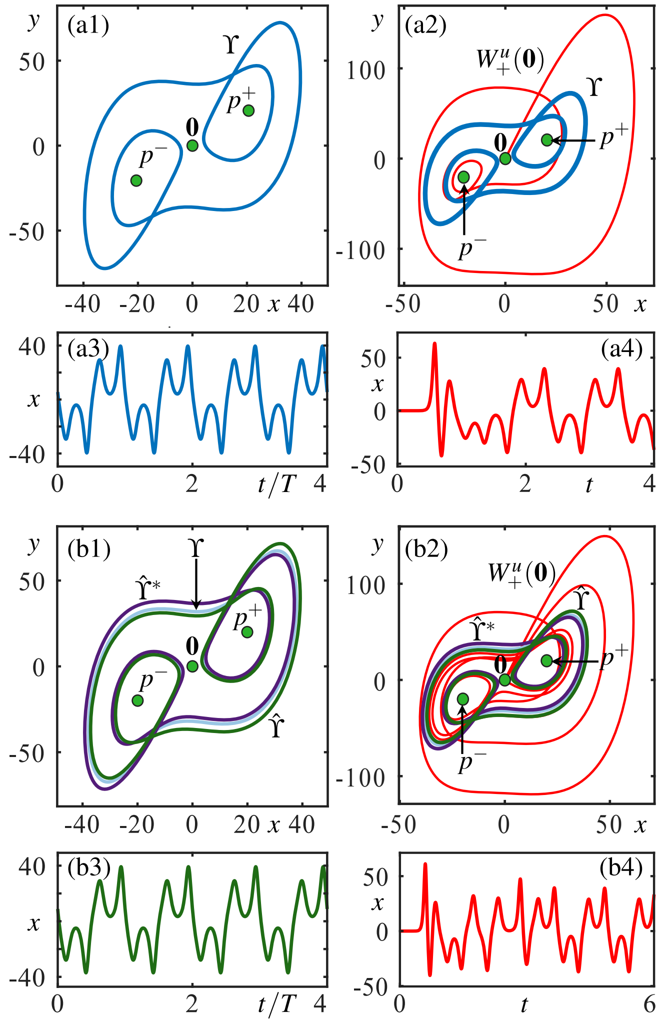

Figure 7: The S-invariant periodic orbit Υ (blue curve), and $W^u_+(\mathbf{0})$ (red curve), shown in panels (a1)–(a4) for $\hat{\rho} = 0.830$ when Υ is attracting, and in panels (b1)–(b4) for $\hat{\rho} = 0.820$ when Υ is a saddle with the coexisting attractors $\hat{\Upsilon}$ and $\hat{\Upsilon}^*$ (green and purple curves); also shown are the three saddle equilibria $\mathbf{0}$ and $p^\pm$ (green dots). Panels (a1),(b1) and (a2),(b2) are projections onto the (x, y)-plane without and with $W^u_+(\mathbf{0})$, respectively; the time series in x of Υ is shown in panel (a3), that of $\hat{\Upsilon}$ in panel (b3), and those of $W^u_+(\mathbf{0})$ in panels (a4),(b4). Compare with Figure 2.

branches can be distinguished in Figure 8(a2). This pair undergoes a further supercritical period-doubling bifurcation $\mathrm{PD}_{\hat{\Upsilon}_2}$ at $\hat{\rho} \approx 0.817$, where it loses stability, and eventually ends in the homoclinic bifurcation Hom_s with $s = \texttt{rllrrllr}$ at $\hat{\rho} \approx 0.574$. Just past $\mathrm{PD}_{\hat{\Upsilon}_2}$ for decreasing $\hat{\rho}$, a period-doubling cascade creates a pair of chaotic attractors near $\hat{\rho} \approx 0.817$, as illustrated by the orbit diagram in the background of panel (a2).

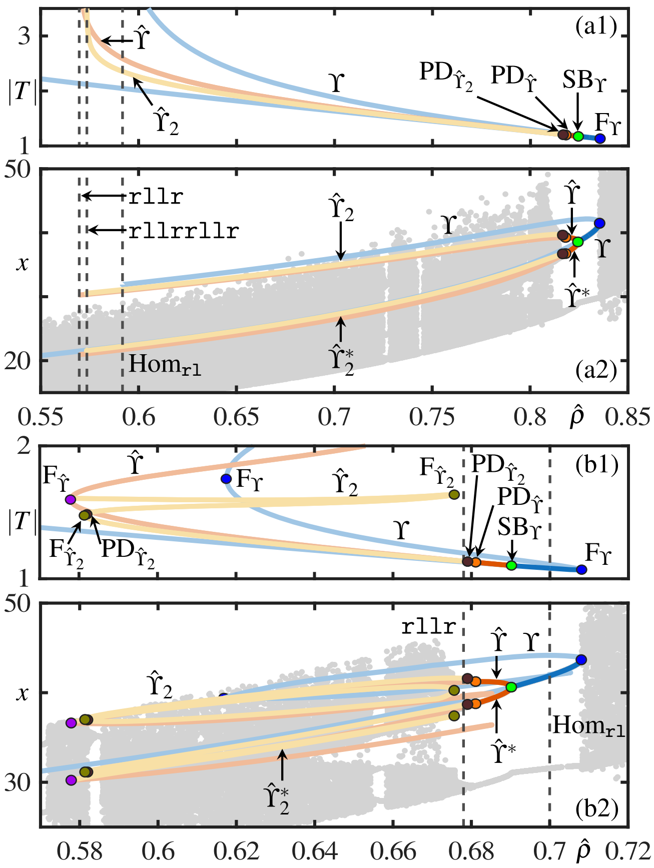

Figure 8: One-parameter bifurcation diagrams in $\hat{\rho}$ for $\hat{\mu} = 0$ (a), and $\hat{\mu} = 0.2$ (b), shown in terms of the period $|T|$ in panels (a1),(b1) and the maximum of x in panels (a2),(b2). Shown are branches of Υ (dark blue when attracting, light blue when a saddle), $\hat{\Upsilon}$, $\hat{\Upsilon}^*$ (dark red when attracting, light red when saddles), and $\hat{\Upsilon}_2$, $\hat{\Upsilon}_2^*$, (dark orange when attracting, light yellow when saddles); also shown are points SB$_{\Upsilon}$ (green) of symmetry-breaking, PD$_{\hat{\Upsilon}}$ (orange) and PD$_{\hat{\Upsilon}_2}$ (black) of period-doubling, and F$_{\Upsilon}$ (blue), F$_{\hat{\Upsilon}}$ (purple), and F$_{\hat{\Upsilon}_2}$ (grey) of fold bifurcation. In the background of panels (a2),(b2) is the orbit diagram (grey points) of the local maxima of x of the attractor at each parameter value.

Figure 8(b) shows the one-parameter bifurcation diagram for $\hat{\mu} = 0.2$. Here we again observe the characteristic folds of periodic orbits associated with Shilnikov-type homoclinic bifurcations. As in panel (a), for increasing $\hat{\rho}$, the attracting periodic orbit Υ disappears at the fold bifurcation F$_{\Upsilon}$ at $\hat{\rho} \approx 0.708$. For decreasing $\hat{\rho}$, the saddle branch of Υ ends at the homoclinic bifurcation Hom$_{\mathtt{rl}}$ at $\hat{\rho} \approx 0.700$. Along the way, this branch also undergoes infinitely many fold bifurcations, as is typical for periodic orbits approaching Shilnikov-type homoclinic bifurcations. We label the first of these fold bifurcations F$_{\Upsilon}$ at $\hat{\rho} \approx 0.617$ near the center of panel (b1). The attracting branch of Υ loses stability at the supercritical symmetry-breaking bifurcation SB$_{\Upsilon}$, now at $\hat{\rho} \approx 0.690$, and subsequently, disappears in the Shilnikov homoclinic bifurcation Hom$_{\mathtt{r}}$ at $\hat{\rho} \approx 0.364$ (not shown, since outside the range).

The pair of attracting asymmetric periodic orbits $\hat{\Upsilon}$ and $\hat{\Upsilon}^*$, created at SB$_{\Upsilon}$, loses stability at the supercritical period-doubling bifurcation PD$_{\hat{\Upsilon}}$ at $\hat{\rho} \approx 0.681$ and then disappears in the homoclinic bifurcation Hom$_{\mathtt{rllr}}$ at $\hat{\rho} \approx 0.678$. Along the way, these periodic orbits undergo a sequence of fold and period-doubling bifurcations with alternating criticality. These bifurcations occur in close succession and are difficult to distinguish on the scale of Figure 8(b); we label only the first fold bifurcation F$_{\hat{\Upsilon}}$ at $\hat{\rho} \approx 0.578$ in panel (b1).

Also visible in Figure 8(b) are the branches of periodic orbits $\hat{\Upsilon}_2$ and $\hat{\Upsilon}_2^*$ that bifurcate from the supercritical period-doubling bifurcation point PD$_{\hat{\Upsilon}}$. They reconnect with $\hat{\Upsilon}$ and $\hat{\Upsilon}^*$ at a (subcritical) period-doubling bifurcation (not labeled), located just past the point F$_{\hat{\Upsilon}}$. Along $\hat{\Upsilon}_2$ and $\hat{\Upsilon}_2^*$, we detect two further period-doubling bifurcations, both labeled PD$_{\hat{\Upsilon}_2}$: one supercritical at $\hat{\rho} \approx 0.679$ and one subcritical at $\hat{\rho} \approx 0.581$.

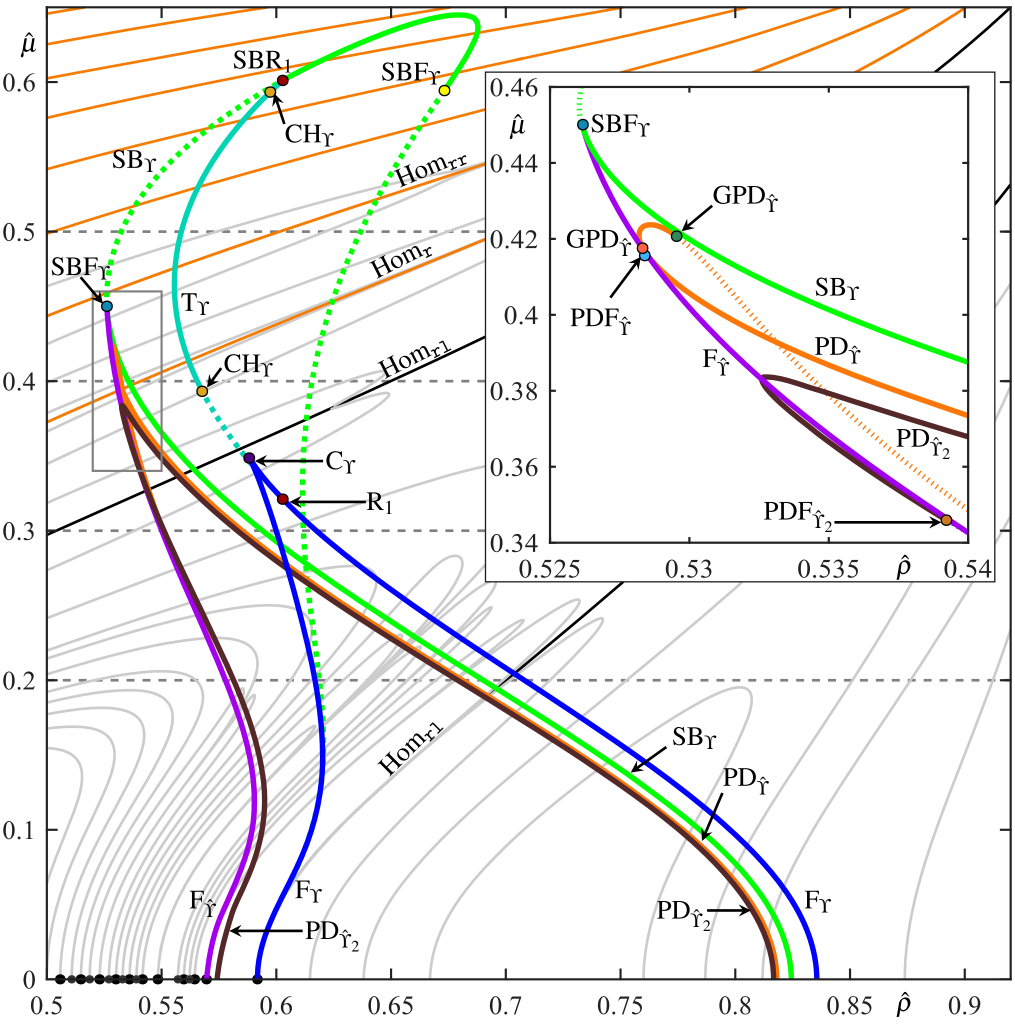

Figure 9: Two-parameter bifurcation diagram in the $(\hat{\rho}, \hat{\mu})$-square with bifurcation curves associated with Υ; shown are the curves F_Υ (blue) and $\mathrm{F}_{\hat{\Upsilon}}$ (light purple) of folds of periodic orbits, SB_Υ (light green solid segments when supercritical, dashed segments when subcritical) of symmetry-breaking, $\mathrm{PD}_{\hat{\Upsilon}}$ (orange) and $\mathrm{PD}_{\hat{\Upsilon}_2}$ (brown) of period-doubling, and T_Υ (light teal solid segments when supercritical, dashed segments when subcritical) of torus bifurcation, together with the codimension-two points SBF_Υ of symmetry-breaking-fold, $\mathrm{PDF}_{\hat{\Upsilon}}$ and $\mathrm{PDF}_{\hat{\Upsilon}_2}$ of fold-flip, $\mathrm{GPD}_{\hat{\Upsilon}}$ of generalized period-doubling, CH_Υ of Chenciner, C_Υ of cusp, R_1 of 1:1 resonance, and SBR_1 of 1:1 resonance of symmetry-breaking bifurcation. The background shows the curves of secondary homoclinic bifurcations. The horizontal dashed line at $\hat{\mu} = 0.2$ corresponds to Figure 8(b), and those at $\hat{\mu} = 0.3$, 0.4, and 0.5 correspond to the one-parameter bifurcation diagrams in Figure 11. The inset provides an enlargement near the codimension-two points $\mathrm{PDF}_{\hat{\Upsilon}}$, $\mathrm{PDF}_{\hat{\Upsilon}_2}$, $\mathrm{GPD}_{\hat{\Upsilon}}$, and SBF_Υ.

In addition, we find two fold bifurcations of periodic orbits, both labeled $\mathrm{F}_{\hat{\Upsilon}_2}$, at $\hat{\rho} \approx 0.581$ and $\hat{\rho} \approx 0.676$. In panel (b2), the spiraling behaviour near the homoclinic bifurcations $\mathrm{Hom}_{\mathtt{r1}}$ and $\mathrm{Hom}_{\mathtt{r1lr}}$ is clearly visible. As before, past the supercritical point $\mathrm{PD}_{\hat{\Upsilon}_2}$, for decreasing $\hat{\rho}$, a period-doubling cascade gives rise to a pair of chaotic attractors.

4.2 Two-parameter bifurcation diagram of Υ

The two-parameter bifurcation diagram of system (1) relating to the periodic orbit Υ is shown in Figure 9 in the overall style of Figure 4. Specifically, Figure 9 shows the codimension-one bifurcation curves F_Υ and $\mathrm{F}_{\hat{\Upsilon}}$ of folds of periodic orbits, SB_Υ of symmetry-breaking bifurcation, and $\mathrm{PD}_{\hat{\Upsilon}}$ and $\mathrm{PD}_{\hat{\Upsilon}_2}$ of period-

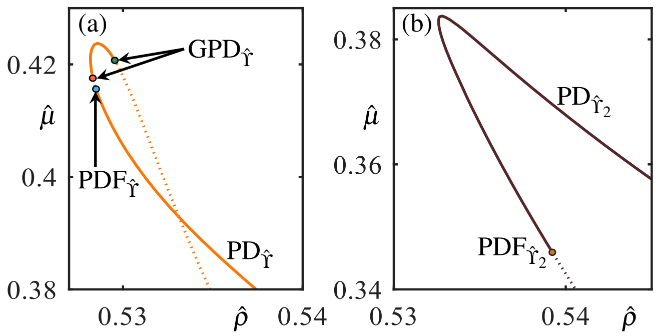

Figure 10: Supercritical (solid) and subcritical (dashed) segments of the period-doubling curves $\mathrm{PD}_{\hat{\Upsilon}}$ in panel (a) and $\mathrm{PD}_{\hat{\Upsilon}_2}$ in panel (b), with bounding codimension-two points $\mathrm{PDF}_{\hat{\Upsilon}}$ and $\mathrm{PDF}_{\hat{\Upsilon}_2}$ of fold-flip, and $\mathrm{GPD}_{\hat{\Upsilon}}$ of generalized period-doubling bifurcation.

doubling bifurcation; they were continued by starting from the respective bifurcation points in Figure 8. The horizontal dashed line at $\hat{\mu} = 0.2$ in Figure 9 corresponds to Figure 8(b), and the additional dashed lines at $\hat{\mu} = 0.3$, 0.4, and 0.5 indicate one-parameter bifurcation diagrams Figure 11, which will be discussed below. Also shown in Figure 9 is the curve T_{Υ} of torus bifurcation, which was continued from a torus bifurcation point detected in the one-parameter continuation for $\hat{\mu} = 0.4$. The inset enlarges the region containing codimension-two bifurcation points involved in changes in criticality of the period-doubling bifurcation $\mathrm{PD}_{\hat{\Upsilon}}$, and of the symmetry-breaking bifurcation SB_{Υ}.

The curve F_{Υ} of fold bifurcation of periodic orbits in Figure 9 emanates from the $\hat{\rho}$-axis at $(\hat{\rho},\hat{\mu}) \approx (0.836, 0)$. For increasing $\hat{\mu}$, it reaches a maximum at a cusp bifurcation C_{Υ} at $(\hat{\rho},\hat{\mu}) \approx (0.588, 0.349)$ and then returns to the $\hat{\rho}$-axis while approaching the curve $\mathrm{Hom}_{\mathtt{r1}}$ of secondary homoclinic bifurcation to end at $(\hat{\rho},\hat{\mu}) \approx (0.592, 0)$. Along the curve F_{Υ}, we identify a 1:1 resonance point R_1 at $(\hat{\rho},\hat{\mu}) \approx (0.603, 0.321)$; see [23] for details of this codimension-two bifurcation.

Continuation of the symmetry-breaking bifurcation SB_{Υ} from Figure 8(a) yields the curve SB_{Υ} in Figure 9. Initially, SB_{Υ} grows with increasing $\hat{\mu}$ but, unlike its counterpart SB_{Γ} of Γ, it reaches a maximum at $(\hat{\rho},\hat{\mu}) \approx (0.679, 0.645)$ and then crosses itself at a single point of self-intersection, before approaching the curve $\mathrm{Hom}_{\mathtt{r1}}$ of secondary homoclinic bifurcation and ending on the $\hat{\rho}$-axis at $(\hat{\rho},\hat{\mu}) \approx (0.592, 0)$. The criticality of the symmetry-breaking bifurcation changes along SB_{Υ} at three codimension-two points. Two of them are symmetry-breaking–fold bifurcation points SBF_{Υ} at $(\hat{\rho},\hat{\mu}) \approx (0.526, 0.450)$ and at $(\hat{\rho},\hat{\mu}) \approx (0.673, 0.594)$, which each give rise to curves of fold bifurcation of periodic orbits that we also continued. In Figure 9, we only show the curve $\mathrm{F}_{\hat{\Upsilon}}$ that ends at the left-most point SBF_{Υ} and corresponds to the fold point $\mathrm{F}_{\hat{\Upsilon}}$ in Figure 8(b); see also the inset. For decreasing $\hat{\mu}$, this curve $\mathrm{F}_{\hat{\Upsilon}}$ ends at $(\hat{\rho},\hat{\mu}) \approx (0.570, 0)$.

The third codimension-two bifurcation point on the curve SB_{Υ} is SBR_1 at $(\hat{\rho},\hat{\mu}) \approx (0.603, 0.601)$, which is a special type of 1:1 resonance point [3]. The symmetry-breaking bifurcation along the curve SB_{Υ} is supercritical from $(\hat{\rho},\hat{\mu}) \approx (0.824, 0)$ up to the left-most point SBF_{Υ}, and again between SBR_1 and the right-most point SBF_{Υ}, and it is subcritical elsewhere. From the point SBR_1 emanates a curve T_{Υ} of torus bifurcation. For decreasing $\hat{\mu}$, it ends at the 1:1 resonance point R_1 on F_{Υ} mentioned above. The torus bifurcation along T_{Υ} changes criticality at two Chenciner points CH_{Υ} [23], which are located at $(\hat{\rho},\hat{\mu}) \approx (0.568, 0.393)$ and $(\hat{\rho},\hat{\mu}) \approx (0.602, 0.601)$. Between these two points, the torus bifurcation is supercritical; otherwise, it is subcritical.

The curve $\mathrm{PD}_{\hat{\Upsilon}}$ of period-doubling bifurcation was continued from the point $\mathrm{PD}_{\hat{\Upsilon}}$ at $(\hat{\rho},\hat{\mu}) \approx (0.818, 0)$ in Figure 8(a). It grows with increasing $\hat{\mu}$, reaches a maximum at $(\hat{\rho},\hat{\mu}) \approx (0.529, 0.424)$, and returns via a single point of self-intersection (see inset) to the $\hat{\rho}$-axis at $(\hat{\rho},\hat{\mu}) \approx (0.570, 0)$, which is the endpoint of the curve $\mathrm{Hom}_{\mathtt{r1lr}}$ of secondary homoclinic bifurcation. Since $\mathrm{PD}_{\hat{\Upsilon}}$ has a self-intersection, there must be codimension-two points on this curve; these are the fold-flip bifurcation $\mathrm{PDF}_{\hat{\Upsilon}}$ at $(\hat{\rho},\hat{\mu}) \approx (0.529, 0.416)$, where $\mathrm{PD}_{\hat{\Upsilon}}$ is tangent to $\mathrm{F}_{\hat{\Upsilon}}$, and two generalized period-doubling bifurcations $\mathrm{GPD}_{\hat{\Upsilon}}$ at $(\hat{\rho},\hat{\mu}) \approx (0.528, 0.418)$ and $(\hat{\rho},\hat{\mu}) \approx (0.530, 0.421)$ (shown in the inset); the latter are associated with the emergence of fold curves

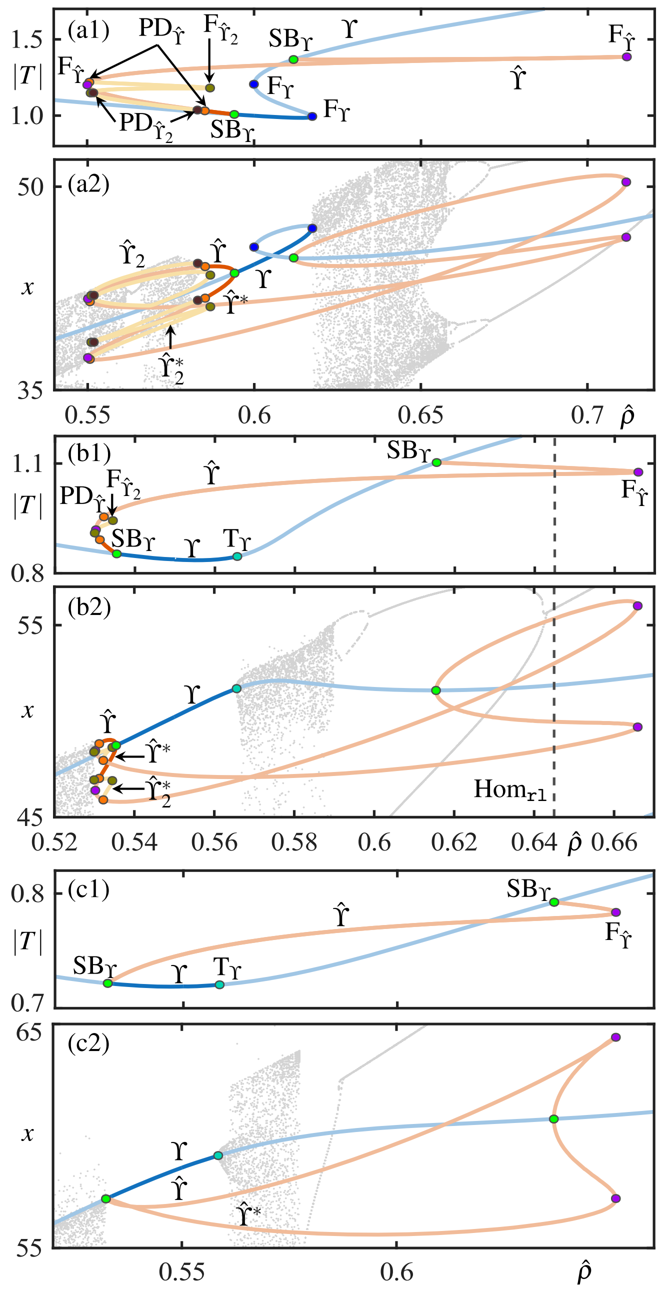

Figure 11: One-parameter bifurcation diagrams in $\hat{\rho}$ for $\hat{\mu} = 0.3$ (a), $\hat{\mu} = 0.5$ (b), and $\hat{\mu} = 0.57$ (c), showing branches of Υ, $\hat{\Upsilon}$, $\hat{\Upsilon}^*$, $\hat{\Upsilon}_2$, $\hat{\Upsilon}_2^*$, and the background orbit diagram in the layout of Figure 8.

$\mathrm{F}_{\hat{\Upsilon}_2}$ of the period-doubled periodic orbit $\hat{\Upsilon}_2$ from Figure 8(b). The period-doubling along $\mathrm{PD}_{\hat{\Upsilon}}$ is supercritical from the point $(\hat{\rho}, \hat{\mu}) \approx (0.818, 0)$ on the $\hat{\rho}$-axis up to $\mathrm{PDF}_{\hat{\Upsilon}}$, as well as between the two points $\mathrm{GPD}_{\hat{\Upsilon}}$, and subcritical otherwise; this is illustrated in Figure 10(a).

Similarly, the curve $\mathrm{PD}_{\hat{\Upsilon}_2}$ was continued from the point $\mathrm{PD}_{\hat{\Upsilon}_2}$ at $(\hat{\rho}, \hat{\mu}) \approx (0.817, 0)$ in Figure 8(a). It grows for increasing $\hat{\mu}$, reaches a maximum at $(\hat{\rho}, \hat{\mu}) \approx (0.533, 0.384)$, and returns to the $\hat{\rho}$-axis at $(\hat{\rho}, \hat{\mu}) \approx (0.574, 0)$. Unlike $\mathrm{PD}_{\hat{\Upsilon}}$, the curve $\mathrm{PD}_{\hat{\Upsilon}_2}$ does not have a point of self-intersection; its criticality changes only once; namely, at the codimension-two point $\mathrm{PDF}_{\hat{\Upsilon}_2}$ at $(\hat{\rho}, \hat{\mu}) \approx (0.539, 0.346)$ (shown in the inset), which gives rise to a fold curve $\mathrm{F}_{\hat{\Upsilon}_2}$ (not shown). As Figure 10(b) shows, the period-doubling along $\mathrm{PD}_{\hat{\Upsilon}_2}$ is supercritical between the points $(\hat{\rho}, \hat{\mu}) \approx (0.817, 0)$ and $\mathrm{PDF}_{\hat{\Upsilon}_2}$, and subcritical otherwise.

The one-parameter bifurcation diagrams along the horizontal lines at $\hat{\mu} = 0.3$, 0.4 and 0.5 in Figure 9 are presented in Figure 11 in the style of Figure 8. Figure 11(a) for $\hat{\mu} = 0.3$ shows that, from the attracting periodic orbit Υ near the middle-left of panel (a1) up to the supercritical period-doubling bifurcation $\mathrm{PD}_{\hat{\Upsilon}_2}$ at $\hat{\rho} \approx 0.583$, the overall bifurcation structure is similar to that for $\hat{\mu} = 0.2$ in Figure 8(b1). However, similar to the transition from Figure 3(b) to Figure 6(a), the branches of asymmetric periodic orbits $\hat{\Upsilon}$ and $\hat{\Upsilon}^*$ in Figure 8(a), created at the supercritical point SB_Υ at $\hat{\rho} \approx 0.594$, no longer end in a homoclinic bifurcation. Instead, they reconnect with Υ at a subcritical point SB_Υ at $\hat{\rho} \approx 0.612$, which is clearly visible near the center of panel (a1). Panel (a2) shows that the fold bifurcation $\mathrm{F}_{\hat{\Upsilon}}$ at $\hat{\rho} \approx 0.617$ lies just below the onset of chaotic dynamics, while a period-doubling cascade from the supercritical period-doubling point $\mathrm{PD}_{\hat{\Upsilon}_2}$ for decreasing $\hat{\rho}$ creates a chaotic attractor.

Figure 11(b) shows the case $\hat{\mu} = 0.4$. For increasing $\hat{\rho}$, the attracting periodic orbit Υ on the left of panel (b1) no longer ends in a fold bifurcation, but instead, loses stability in the supercritical torus bifurcation T_Υ at $\hat{\rho} \approx 0.565$, before disappearing in the homoclinic bifurcation $\mathrm{Hom}_{\mathtt{r1}}$ at $\hat{\rho} \approx 0.844$. For decreasing $\hat{\rho}$, the asymmetric periodic orbits $\hat{\Upsilon}$ and $\hat{\Upsilon}^*$, created at the supercritical bifurcation point SB_Υ at $\hat{\rho} \approx 0.535$, lose stability in the supercritical bifurcation point $\mathrm{PD}_{\hat{\Upsilon}}$ at $\hat{\rho} \approx 0.531$ and later reconnect with Υ via a subcritical bifurcation point SB_Υ at $\hat{\rho} \approx 0.615$. The newly born period-doubled periodic orbits $\hat{\Upsilon}_2$ and $\hat{\Upsilon}_2^*$ undergo two fold bifurcations $\mathrm{F}_{\hat{\Upsilon}_2}$ before reconnecting with the branches of $\hat{\Upsilon}$ and $\hat{\Upsilon}^*$ at the subcritical points $\mathrm{PD}_{\hat{\Upsilon}}$. No further period-doubling bifurcations are detected on these branches. As shown in panel (b2), the torus bifurcation lies just below the onset of chaotic dynamics. Unlike for $\hat{\mu} = 0.3$, no period-doubling cascade occurs on the left-hand side of panel (b2); nevertheless, a chaotic attractor appears just below the fold bifurcation $\mathrm{F}_{\hat{\Upsilon}}$ at $\hat{\rho} \approx 0.530$.

Lastly, Figure 11(c) shows one-parameter bifurcation diagram for $\hat{\mu} = 0.5$. The symmetry-breaking bifurcation SB_Υ at $\hat{\rho} \approx 0.532$ on the left side of the figure has changed criticality and is now subcritical. As a result, the asymmetric periodic orbits $\hat{\Upsilon}$ and $\hat{\Upsilon}^*$ that exist to the right of SB_Υ are of saddle type. No period-doubling bifurcations are found along these branches, which instead, reconnect with Υ at a second subcritical point SB_Υ at $\hat{\rho} \approx 0.637$. Panel (c2) shows that the supercritical torus bifurcation T_Υ at $\hat{\rho} \approx 0.559$ marks the onset of chaotic dynamics for $\hat{\rho} > 0.559$. In contrast with the previous cases, there the left-hand symmetry-breaking bifurcation SB_Υ lies close to the region where the chaotic attractor appears.

5 Bifurcations of Γ and Υ in relation to the kneading diagram and Lyapunov spectrum

We now discuss how the bifurcation curves associated with the S-invariant periodic orbits Γ and Υ relate to the overall dynamics of system (1). To this end, we consider two complementary perspectives: the topological viewpoint, characterized by the kneading diagrams as in Figure 1(a), and the dynamical viewpoint of identifying different types of attractors via the Lyapunov spectrum. Figure 12 shows the bifurcation curves associated with Γ from Figure 4 and those associated with Υ from Figure 9 together with the kneading diagram of K_9 (now in pastel color) with curves of secondary homoclinic bifurcation for the first few symbol sequences.

To provide the second perspective, Figure 13 shows the bifurcation curves associated with Γ and Υ in the $(\hat{\rho}, \hat{\mu})$-square colored by the Lyapunov spectrum computed along $W^u_+(\mathbf{0})$; in this way, we identify different regions where $W^u_+(\mathbf{0})$ approaches an equilibrium point (E), a periodic orbit (P), or a chaotic attractor. As in [31], we distinguish between a quasiattractor (CQ), which is chaotic but not robust due to the existence of periodic windows, and a pseudohyperbolic attractor (CP), which is a robust chaotic attractor that is potentially wild. These different types of attractors are identified in Figure 13 by their Lyapunov spectrum as listed in Table 1; note that we also consider and show a boundary case (BW) for which this difference cannot be decided within the accuracy of the computation (as specified by the threshold parameter ε). More specifically, for each parameter point on a uniform 400×600 grid over the ranges $0.5 \leq \hat{\rho} \leq 0.92$ and $0 \leq \hat{\mu} \leq 0.65$, we compute $W^u_+(\mathbf{0})$ by integration with the `MATLAB` function `ode45` over the time interval $[0, 300]$ for the initial condition at distance 0.1 along the unstable eigenvector from $\mathbf{0}$. All four Lyapunov exponents are computed simultaneously from the linearized system with Gram–Schmidt orthonormalization as implemented in [9]. We use $\varepsilon = 0.05$ throughout as the threshold parameter that accounts for known

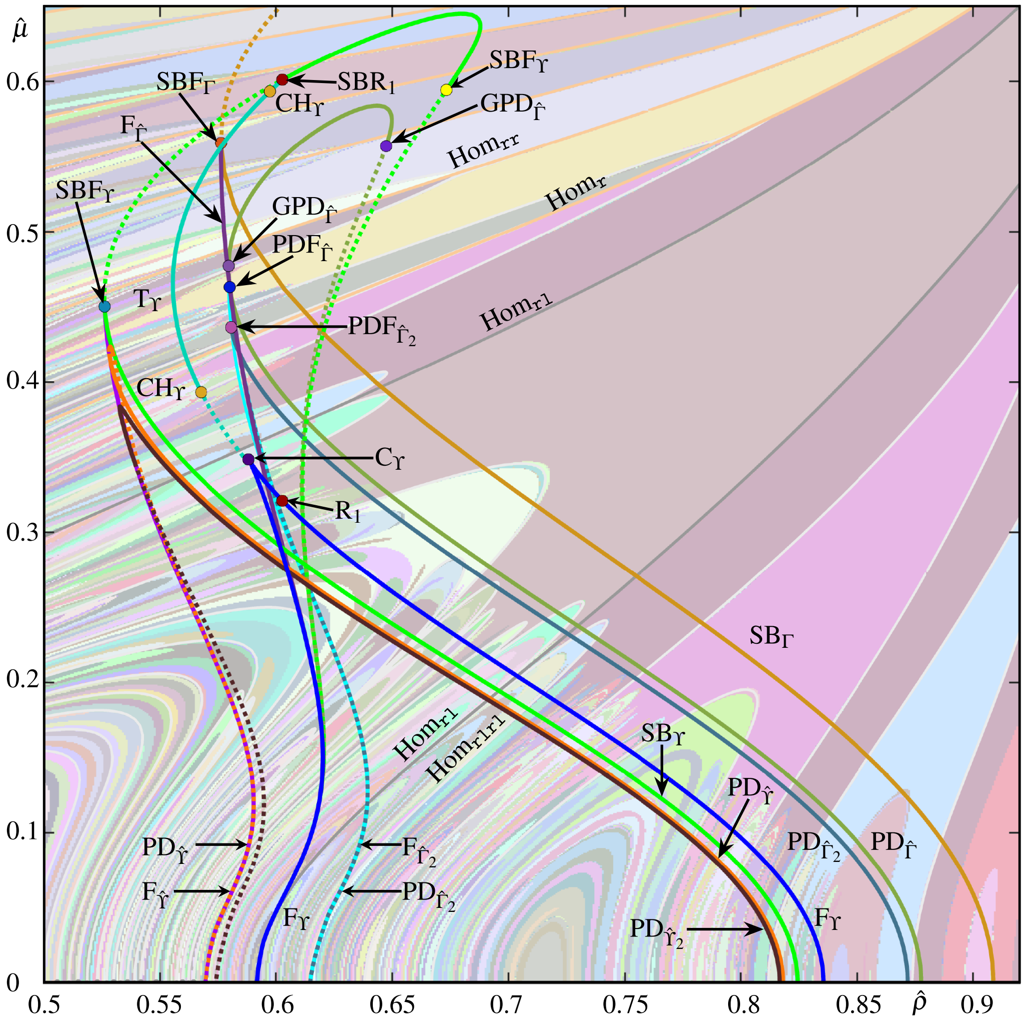

Figure 12: The bifurcation curves associated with Γ and Υ from figures 4 and 9, shown in the $(\hat{\rho}, \hat{\mu})$-square colored by the kneading diagram of K_9 with curves of secondary homoclinic bifurcation.

numerical limitations in the computation of the Lyapunov spectrum. This value was determined as the smallest value for which at least one Lyapunov exponent satisfies $|\Lambda_i| < \varepsilon$ at all non-equilibrium parameter points, and the sum of the four Lyapunov exponents lies within 10^{-4} of the exact value $-49/3$ given as the (constant) trace of the Jacobian matrix; see [31] for a detailed discussion of these validation criteria.

Notice in Figures 12 and 13 that the supercritical segments of the bifurcation curves associated with Γ and Υ extend from the $\hat{\rho}$-axis roughly in parallel. These curves pass near the 'tips' of several finger-like structures in the kneading diagram of Figure 12, albeit without perfect alignment. This is reminiscent of the bifurcation structure of the *driven–dissipative Bose–Hubbard dimer* found in [14], which is another example of a four-dimensional vector field with $\mathbb{Z}_2$-symmetry [15]; more specifically, certain bifurcation curves of S-invariant periodic orbits align quite closely with similar regions of accumulating finger-like structures that are bounded by curves of Shilnikov homoclinic bifurcation. Moreover, these parallel curve segments form the boundaries of 'periodic stripes' (blue) identified by the Lyapunov spectrum in Figure 13, which are the extensions for $\mu > 0$ of the respective periodic windows known from the Lorenz system. Two such stripes can clearly be distinguished: a large region on the right with periodic dynamics, where mainly the basic S-invariant periodic orbit Γ is the attractor; and a narrower stripe in the center, where mainly the S-invariant periodic orbit Υ is the attractor.

All these bifurcation curves of all these bifurcations — be they super- or subcritical — appear to be

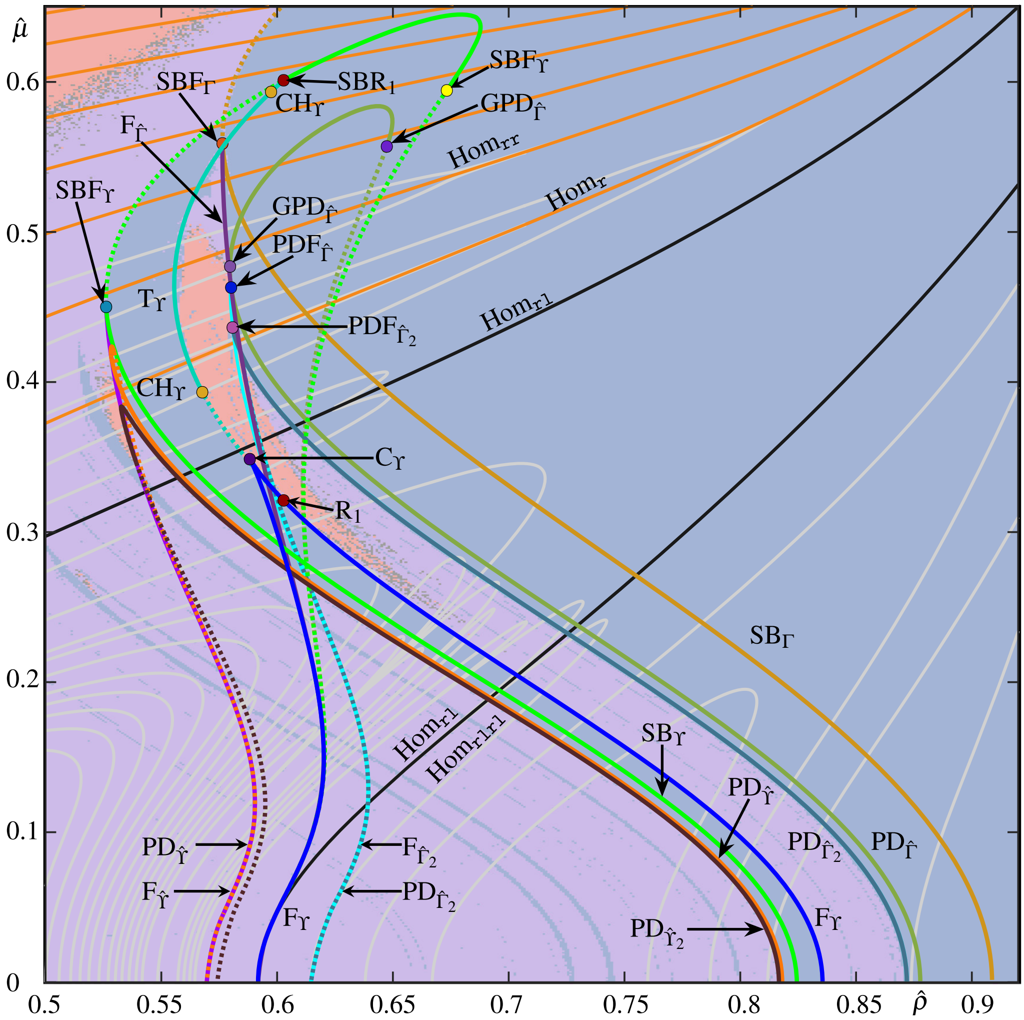

Figure 13: The bifurcation curves associated with Γ and Υ from figures 4 and 9, shown in the $(\hat{\rho}, \hat{\mu})$-square colored by the Lyapunov spectrum computed along $W^u_+(\mathbf{0})$, with regions distinguished as listed in Table 1 by whether the attractor is: (P) periodic (blue); (CQ) a quasiattractor (lavender); (CP) a pseudohyperbolic attractor (salmon); or (BW) a boundary case (grey) between (CQ) and (CP).

case	criterion	attractor	color
(E)	$\Lambda_1 < -\varepsilon$	equilibrium	green
(P)	$\lvert\Lambda_1\rvert < \varepsilon, \quad \Lambda_2 < -\varepsilon$	periodic orbit	blue
(CQ)	$\Lambda_1 > \varepsilon, \quad \lvert\Lambda_2\rvert < \varepsilon, \quad \Lambda_3 < -\varepsilon, \quad S_3 < -\varepsilon$	quasiattractor	lavender
(BW)	$\Lambda_1 > \varepsilon, \quad \lvert\Lambda_2\rvert < \varepsilon, \quad \Lambda_3 < -\varepsilon, \quad \lvert S_3\rvert < \varepsilon$	undecided boundary case	grey
(CP)	$\Lambda_1 > \varepsilon, \quad \lvert\Lambda_2\rvert < \varepsilon, \quad \Lambda_3 < -\varepsilon, \quad S_3 > \varepsilon$	pseudohyperbolic	salmon

Table 1: Numerical classification of the Lyapunov spectrum computed along $W^u_+(\mathbf{0})$ as introduced in [31]; here S_3 is the sum of the three largest Lyapunov exponents. The corresponding color coding used in Figure 13 was obtained for $\varepsilon = 0.05$.

nested with respect to one another in the region $0.5 < \hat{\rho} < 0.65$ and $0.3 < \hat{\mu} < 0.6$. In particular, the loop formed by SB$_\Upsilon$ encloses the loops of period-doubling bifrucations of Γ, and all codimension-two bifurcation points of Γ and Υ lie within this region.

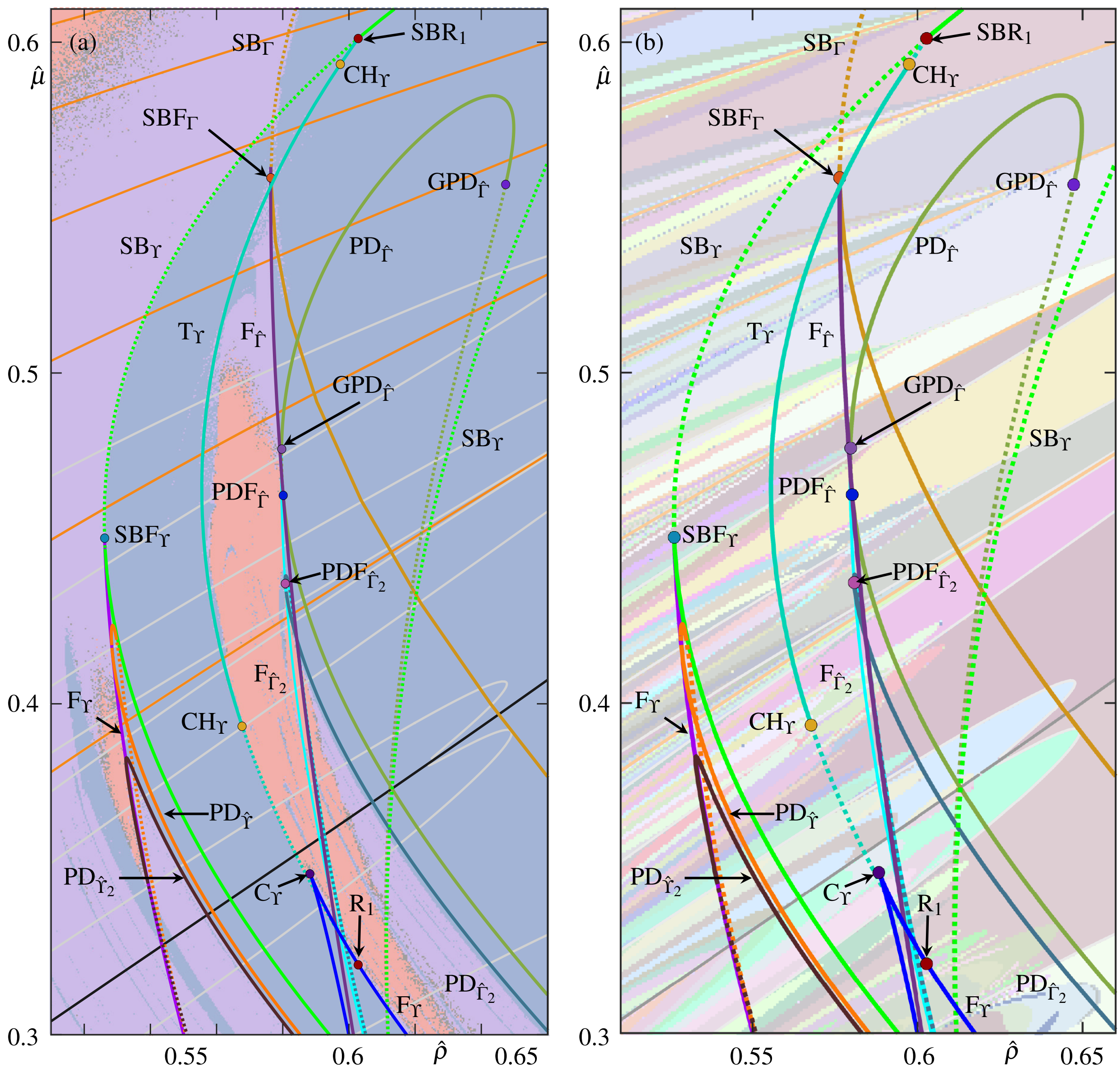

Figure 14: The bifurcation curves associated with Γ and Υ in the part of the $(\hat{\rho},\hat{\mu})$-square with $0.51 \leq \hat{\rho} \leq 0.66$ and $0.30 \leq \hat{\mu} \leq 0.61$, colored by the Lyapunov spectrum computed along $W^u_+(\mathbf{0})$ in panel (a) and the kneading diagram of K_9 in panel (b), both computed over a 350×720 grid. Compare with Figures 12 and 13.

A particular feature in Figure 13 is a region (CP) where the chaotic attractor is pseudohyperbolic. Figure 14 shows enlargements near this region; here the Lyapunov spectrum computed along $W^u_+(\mathbf{0})$ in panel (a) and the kneading diagram of K_9 in panel (b) have been computed over a uniform grid with 350×720 points over the range shown. The curve T_Υ of torus bifurcation appears to form part of the left boundary of the central region with a pseudohyperbolic attractor in Figure 14(a). This observation is consistent with earlier findings in [31], where a curve of torus bifurcation similarly appears to be involved in the transition from periodic to pseudohyperbolic chaotic dynamics. As discussed in [31], the torus bifurcation does not in itself form this kind of boundary; rather, the appearance of a pseudohyperbolic attractor is likely the result of a potentially complicated sequence of nearby bifurcations associated with overlapping resonance tongues. Other parts of the boundary of this region with a pseudohyperbolic attractor are less evident. The fold curves $\mathrm{F}_{\hat{\Gamma}}$ and $\mathrm{F}_{\hat{\Gamma}_2}$ appear to play a role, but no single curve provides a clear boundary. Likewise, the transitions to a chaotic quasiattractor (CQ) above and below this region do not correspond to identified bifurcation curves.

A natural question concerns the topological ingredient for wild chaos, namely, the density of homoclinic bifurcations. A comparison with Figure 14(b) shows that in the region where pseudohyperbolic chaotic dynamics exist there does not appear to be a dense accumulation of Shilnikov-homoclinic bifurcations throughout. Instead, this density requirement for wild chaos seems to be satisfied only in smaller, localized subregions. More specifically, the kneading diagram of K_9 reveals multiple finger-like structures of increasing complexity, interspersed with comparatively broad regions of constant kneading invariant. Hence, it is possible that wild chaotic attractors exist within these smaller subregions, but the current evidence remains somewhat inconclusive.

Notice in Figure 14(a) that there is a second, smaller region to the left of the curve $\mathrm{F}_{\hat{\Upsilon}}$, where the existence of a pseudohyperbolic attractor is detected by the Lyapunov spectrum. Comparison with panel (b) suggests that Shilnikov homoclinic bifurcations might be dense in at least some parts of these two regions. Since this smaller region lies in between two periodic stripes in much the same way as the larger central region, there may be an infinite sequence of ever smaller regions with a pseudohyperbolic attractor, in between increasingly thinner periodic stripes.

6 Conclusions

We presented bifurcation curves of the S-invariant periodic orbits Γ and Υ of system (1) in the compactified $(\hat{\rho},\hat{\mu})$-square. We identified two distinct roles of the bifurcation curves by comparing them with the Lyapunov spectrum and the kneading diagram computed along $W^u_+(\mathbf{0})$. On the one hand, they mediate transitions between regions of periodic dynamics, where Γ or Υ are attracting, and regions of quasiattractor chaotic dynamics (CQ) caused by period-doubling cascades. On the other hand, they delimit successively smaller parameter regions where the Lyapunov spectrum satisfies the necessary condition for pseudohyperbolic chaotic dynamics (CP). Notably, the curve T_Υ of torus bifurcation plays a role in bounding these regions, in analogy with the case of the wild pseudohyperbolic attractor from [17] studied in [31]. The kneading diagram suggests that curves of different Shilnikov homoclinic bifurcations are also dense at least in certain parts of these regions, so that the required conditions for the existence of a wild chaotic attractor are satisfied.

We found that the bifurcation curves of Γ and Υ are arranged in the $(\hat{\rho},\hat{\mu})$-square in a nested manner and are closely interrelated. For small values of $\hat{\mu}$, the supercritical segments of the symmetry-breaking bifurcations for both Γ and Υ and period-doubling bifurcations of $\hat{\Gamma}$, $\hat{\Gamma}_2$, $\hat{\Upsilon}$ and $\hat{\Upsilon}_2$, together with the fold bifurcation of Υ, extend across the parameter plane and broadly follow the alignment of the finger-like structures in the kneading diagram, albeit without direct correspondence. The arrangement of the bifurcation curves becomes especially intricate in the region $0.5 < \hat{\rho} < 0.65$ and $0.3 < \hat{\mu} < 0.6$, which also contains all codimension-two bifurcation points of Γ and Υ.

In the Bose–Hubbard dimer [14], the S-invariant periodic orbits undergo a well-defined sequence of symmetry-breaking, period-doubling, and symmetry-increasing bifurcations, which sharply align with the boundaries of chaotic dynamics and accumulating curves of homoclinic bifurcation. In comparison, system (1) does not exhibit such a precise alignment. Here, the boundaries between regions of constant kneading invariant and accumulating curves of homoclinic bifurcation are less defined, and a symmetry-increasing bifurcation of chaotic attractors has not been detected. It remains an open question whether such a bifurcation exists in system (1), and whether it could serve as a boundary of chaotic dynamics and accumulating fingers of different Shilnikov homoclinic bifurcations.

The results we presented here may serve as motivation for further exploration of wild chaotic dynamics in higher-dimensional vector fields. Regarding the Lorenz-like system (1) itself, an interesting challenge is to find so-called robust heterodimensional cycles between periodic orbits of different index, that is, with different dimensions of their unstable manifolds. The existence of these objects follows from the robust existence of Shilnikov homoclinic bifurcations [24, 26, 25]; coexisting periodic orbits of different index are clearly present and finding the required connecting orbits is the subject of ongoing work. We plan to find such cycles with advanced numerical methods, including Lin's method; that this is feasible was demonstrated for the, as yet, only example of a four-dimensional vector field with known heterodimensional cycles, the so-called Atri model for cellular calcium dynamics [39, 20, 38]. Finding heterodimensional cycles also in (1) would be a way of making a connection between wild chaotic attractors and wild invariant saddle-type sets [7, 6]. More generally, the combination of numerical techniques employed here can be brought to bear also in the exploration of other ‘exotic’ types of dynamics in any vector field of interest.

Acknowledgments

The authors would like to thank Roberto Barrio, Rodrigues Bitha, Andrus Giraldo, and Dmitry Turaev for helpful discussions. This work has been supported by Royal Society Te Apārangi Marsden Fund grant #22-UOA-204.

References

[1] A. Abad, R. Barrio, F. Blesa, and M. Rodríguez. Algorithm 924: TIDES, a Taylor series integrator for differential equations. *ACM Transactions on Mathematical Software*, 39(1):1–28, 2012.

[2] V. S. Afraimovich, V. V. Bykov, and L. P. Shilnikov. On the origin and structure of the Lorenz attractor. *Doklady Akademii Nauk SSSR*, 234:336–39, 1977.

[3] Antonio Algaba, Manuel Merino, and Alejandro Rodríguez-Luis. Takens–Bogdanov bifurcations of periodic orbits and Arnold’s tongues in a three-dimensional electronic model. *International Journal of Bifurcation and Chaos*, 11(2):513–31, 2001.

[4] R. Barrio, F. Blesa, and S. Serrano. Behavior patterns in multiparametric dynamical systems: Lorenz model. *International Journal of Bifurcation and Chaos*, 22(06), 2012.

[5] R. Barrio, A. Shilnikov, and L. P. Shilnikov. Kneadings, symbolic dynamics and painting Lorenz chaos. *International Journal of Bifurcation and Chaos*, 22(04), 2012.

[6] C. Bonatti, L. J. Díaz, and M. Viana. *Dynamics Beyond Uniform Hyperbolicity. A Global Geometric and Probabilistic Perspective*. Springer, New York, 2005.

[7] Christian Bonatti and Lorenzo J. Díaz. Persistent nonhyperbolic transitive diffeomorphisms. *Annals of Mathematics*, 143(2):357–96, 1996.

[8] V. V. Bykov and A. Shilnikov. On the boundaries of the domain of existence of the Lorenz attractor. *Sel. Math. Sov.*, 11:375–82, 1992.

[9] F. Christiansen and H. H. Rugh. Computing Lyapunov spectra with continuous Gram-Schmidt orthonormalization. *Nonlinearity*, 10(5):1063–72, 1997.

[10] Jennifer L. Creaser, B. Krauskopf, and H. M. Osinga. Finding first foliation tangencies in the Lorenz system. *SIAM J. Appl. Dyn. Syst.*, 16(4):2127–64, 2017.

[11] E. J. Doedel. AUTO: A program for the automatic bifurcation analysis of autonomous systems. *Congressus Numerantium*, 30(265–84):25–93, 1981.

[12] E. J. Doedel. AUTO-07p: Continuation and bifurcation software for ordinary differential equations with major contributions from Champneys A R, Fairgrieve T F, Kuznetsov Yu A, Oldeman B E, Paffenroth R C, Sandstede B, Wang X J and Zhang C, 2007.

[13] H. R. Dullin, S. Schmidt, P. H. Richter, and S. K. Grossmann. Extended phase diagram of the Lorenz model. *International Journal of Bifurcation and Chaos*, 17(09):3013–33, 2007.

[14] A. Giraldo, N. G. R. Broderick, and B. Krauskopf. Chaotic switching in driven-dissipative Bose-Hubbard dimers: When a flip bifurcation meets a T-point in $\mathbb{R}^4$. *Discrete and Continuous Dynamical Systems*, 27(7):4023–75, 2022.

[15] A. Giraldo, B. Krauskopf, N. G. R. Broderick, J. A. Levenson, and A. M. Yacomotti. The driven-dissipative Bose–Hubbard dimer: Phase diagram and chaos. *New Journal of Physics*, 22(4), 2020.

[16] A. Gonchenko, S. Gonchenko, A. Kazakov, and A. Kozlov. Elements of contemporary theory of dynamical chaos: A tutorial. Part I. Pseudohyperbolic attractors. *International Journal of Bifurcation and Chaos*, 28(11), 2018.

[17] S. Gonchenko, A. Kazakov, and D. V. Turaev. Wild pseudohyperbolic attractor in a four-dimensional Lorenz system. *Nonlinearity*, 34:2018–47, 2021.

[18] J. Guckenheimer. A strange, strange attractor. In J. E. Marsden and M. McCracken, editors, *The Hopf Bifurcation and Its Applications*, Applied Mathematical Sciences, pages 368–81. Springer, 1976.

[19] J. Guckenheimer and R. F. Williams. Structural stability of Lorenz attractors. *Publications Mathématiques de l'IHÉS*, 50:59–72, 1979.

[20] A. Hammerlindl, B. Krauskopf, G. Mason, and H. M. Osinga. Determining the global manifold structure of a continuous-time heterodimensional cycle. *J. Comput. Dyn.*, 9:393–419, 2022.

[21] J. L. Kaplan and J. A. Yorke. Preturbulence: A regime observed in a fluid flow model of lorenz. *Commun. Math. Phys.*, 67:93–108, 1979.

[22] B. Krauskopf and T. Rieß. A Lin's method approach to finding and continuing heteroclinic connections involving periodic orbits. *Nonlinearity*, 21(8):1655–90, 2008.

[23] Y. A. Kuznetsov. *Elements of Applied Bifurcation Theory*. Springer, 4 edition, 2018.

[24] D. Li. Homoclinic bifurcations that give rise to heterodimensional cycles near a saddle-focus equilibrium. *Nonlinearity*, 30:173–206, 2017.

[25] D. Li, X. Li, Shinohara K., and D. V. Turaev. Robust heterodimensional cycles in two-parameter unfolding of homoclinic tangencies. *arXiv Preprint*, pages 2203.14075,, 2024.

[26] D. Li and D. V. Turaev. Persistence of heterodimensional cycles. *Invent. Math.*, 236:1413–504, 2024.

[27] Xiao-Biao Lin. Using Melnikov's method to solve Silnikov's problems. *Proceedings of the Royal Society of Edinburgh Section* A *Mathematics*, 116(3–4):295–325, 1990.

[28] E. N. Lorenz. Deterministic nonperiodic flows. *Journal of the Atmospheric Sciences*, 20:130–41, 1963.

[29] E. N. Lorenz. Noisy periodicity and reverse bifurcation. In P Cvitanovic, editor, *Universality in Chaos*, pages 292–301. Routledge, 2 edition, 2017.

[30] I. Ovsyannikov, J. D. M. Rademacher, R. Welter, and B. Y. Lu. Time averages and periodic attractors at high Rayleigh number for Lorenz-like models. *Journal of Nonlinear Science*, 33, 2023.

[31] Juan Patiño-Echeverría, Bernd Krauskopf, and Hinke M. Osinga. Global bifurcation structure of a four-dimensional lorenz-like system with a wild chaotic attractor. *Nonlinearity*, 39:065010, 2026.

[32] K. A. Robbins. Periodic solutions and bifurcation structure at high r in the Lorenz model. *SIAM Journal on Applied Mathematics*, 36(3):457–72, 1979.

[33] L. P. Shilnikov, A. Shilnikov, D. V. Turaev, and L. O. Chua. *Methods of Qualitative Theory in Nonlinear Dynamics, Part 2*, volume 5 of *Nonlinear Science Series* A. World Scientific, 1998.

[34] C. Sparrow. *The Lorenz Equations: Bifurcations, Chaos and Strange Attractors*. Applied Mathematical Sciences. Springer, 1982.

[35] W. Tucker. The Lorenz attractor exists. *C. R. Acad. Sci. Ser. I Math.*, 328(12):1197–202, 1999.

[36] D. V. Turaev. A geometric model for pseudohyperbolic Shilnikov attractors. *Regular and Chaotic Dynamics*, 30:174–87, 2025.

[37] D. V. Turaev and L. P. Shilnikov. An example of a wild strange attractor. *Matematicheskii Sbornik*, 189(2):291–314, 1998.

[38] N. Wong, B. Krauskopf, and H. M. Osinga. Cascades of heterodimensional cycles via period doubling. *Commun. Nonlinear Sci. Numer. Simul.*, 140:108328, 2025.

[39] Wenjun Zhang, Bernd Krauskopf, and Vivien Kirk. How to find a codimension-one heteroclinic cycle between two periodic orbits. *Discrete and Continuous Dynamical Systems*, 32(8):2825–51, 2012.